THESIS FOR THE DEGREE OF DOCTOR OF PHILOSOPHY IN THERMO AND FLUID DYNAMICS

On the Aerodynamic Design of the Boxprop

ALEXANDRE CAPITAO PATRAO

Department of Mechanics and Maritime Sciences
Division of Fluid Dynamics
CHALMERS UNIVERSITY OF TECHNOLOGY

Gothenburg, Sweden 2018

On the Aerodynamic Design of the Boxprop
ALEXANDRE CAPITAO PATRAO
ISBN 978-91-7597-795-9

Doktorsavhandlingar vid Chalmers tekniska högskola
Ny serie nr. 4476
ISSN 0346-718X
Department of Mechanics and Maritime Sciences
Division of Fluid Dynamics
Chalmers University of Technology
SE-412 96 Gothenburg
Sweden
Telephone: +46 (0)31-772 1000

Cover:
A counter-rotating open rotor featuring the Boxprop as its front rotor. Flow goes from left to right.

Chalmers Reproservice
Gothenburg, Sweden 2018

On the Aerodynamic Design of the Boxprop
Thesis for the degree of Doctor of Philosophy in Thermo and Fluid Dynamics
ALEXANDRE CAPITAO PATRAO
Department of Mechanics and Maritime Sciences
Division of Fluid Dynamics
Chalmers University of Technology

Abstract

Economic factors and environmental awareness are driving the evolution of aircraft engines towards increasingly lower fuel consumption and emissions. The Counter-Rotating Open Rotor (CROR) is actively being researched around the world, promising a significantly increased propulsion efficiency relative to existing turbofans by employing two, unducted, counter-rotating propeller blade rows, thereby increasing the bypass ratio of the engine and decreasing nacelle drag. Historically, these engines have been plagued by high noise levels, mainly due to the impingement of the front rotor tip vortices on the rear rotor. In modern designs, the noise levels have been decreased by clipping the rear, counter-rotating propeller. This comes at a cost of decreased efficiency.

An alternative, potential solution lies with the Boxprop, which was invented by Richard Avellán and Anders Lundbladh. The Boxprop consists of blade pairs joined at the tip, and is conceptually similar to a box wing. This type of propeller could weaken or eliminate the tip vortex found in conventional blades, thereby reducing the acoustic signature.

This thesis summarizes advances done in the research regarding the aerodynamics of the Boxprop. Aerodynamic optimization of the Boxprop has shown that it features higher propeller efficiency than conventional propellers with the same number of blades, but lower propeller efficiency than conventional propellers with twice as many blades. A key design feature of optimal Boxprop designs is the sweeping of the blade halves in opposite directions. This reduces the interference between the blades and allows the Boxprop to achieve aerodynamic loading where it is most efficient - close to the tip.

A Wake Analysis Method (WAM) is presented in this work which provides a detailed breakdown and quantification of the aerodynamic losses in the flow. It also has the ability to distinguish and quantify the kinetic energy of the tip vortices and wakes. The Wake Analysis Method has been used to analyse both Boxprop blades and conventional propeller blades, and insights from it led to a geometric parametrization and an optimization effort which increased the Boxprop propeller efficiency by 7 percentage points.

Early Boxprop blades did not feature a tip vortex since aerodynamic loading near the tip was relatively low. The optimized Boxprop blades have increased the aerodynamic loading near the tip and this has resulted in a vortex-like structure downstream of the Boxprop at cruise conditions. This vortex is significantly weaker and of different origin than the tip vortex of a conventional propeller.

A CROR featuring the Boxprop as its front rotor (BPOR) has been designed and its performance at cruise is competitive with other published CRORs, paving the way for future work regarding take-off performance and acoustics.

Keywords: Open Rotors, Propfans, Propellers, CROR, CFD, Optimization, Propeller Design, Tip vortex, Wake Analysis Method

List of publications

This thesis is based on the work contained in the following publications:

I R. Avellán, A. Capitao Patrao, A. Lundbladh, and T. Grönstedt, 2015, "Preparing for Proof-of-Concept of a Novel Propeller for Open Rotor Engines", *22nd ISABE Conference*, October 25–30, Phoenix, USA.

II A. Capitao Patrao, R. Avellán, A. Lundbladh, and T. Grönstedt, 2016, "Wake and Loss Analysis for a Double Bladed Swept Propeller", *Proceedings of ASME Turbo Expo 2016*, June 13–17, Seoul, South Korea.

III A. Capitao Patrao, G. Montero Villar, J. Takachi Tomita, C. Bringhenti, R. Avellan, A. Lundbladh, and T. Grönstedt. "An Optimization Platform for High Speed Propellers", *Aerospace Technology Congress*, 11-12 October 2016, Solna, Stockholm.

IV Andersson, J., Eslamdoost, A., Patrao, A. C., Hyensjö, M., and Bensow, R. E. "Energy Balance Analysis of a Propeller in Open Water", *Ocean Engineering*, 158, 162-170, 2018.

V A. Capitao Patrao, T. Grönstedt, R. Avellán, and A. Lundbladh. "Wake Energy Analysis Method Applied to the Boxprop Propeller Concept", *Aerospace Science and Technology*, 2018.

VI A. Capitao Patrao, D. Lindblad, A. Lundbladh, and T. Grönstedt. "Aerodynamic and Aeroacoustic Comparison of Optimized High-Speed Propellers Blades", *Joint Propulsion Conference 2018*, 7-12 July 2018, Cincinnati, OH, United States.

VII A. Capitao Patrao, T. Grönstedt, A. Lundbladh, and G. Montero Villar. "Wake Analysis of an Aerodynamically Optimized Boxprop High Speed Propeller", *Submitted to Journal of Turbomachinery on the 16th of August 2018*

Other relevant publications:

VIII A. Capitao Patrao, "Implementation of Blade Element Momentum/Vortex Methods for the Design of Aero Engine Propellers," Tech. rep., 2017:06.

IX V. Tavares Silva, L. Moraes da Silva, J. Takachi Tomita, C. Bringhenti, T. Grönstedt, A. Capitao Patrao, and O. Petit, 2017, "Numerical Simulation of Nacelle Flowfield for Counter-Rotating Open Rotor Propellers", *23rd ISABE Conference*, September 3–8, Manchester, United Kingdom.

X Lindblad, D., Montero Villar, G., Andersson, N., Capitao Patrao, A., Courty-Audren, S. K., and Napias, G. (2018). "Aeroacoustic Analysis of a Counter Rotating Open Rotor based on the Harmonic Balance Method". *In 2018 AIAA Aerospace Sciences Meeting*, (p. 1004).

Acknowledgements

Not everyone has the opportunity and luxury to work in a field in which they are passionately interested. For this I would like to extend my gratitude towards my supervisor Tomas Grönstedt. Likewise, I would also like to thank him for his advice and counsel throughout my doctoral studies.

I am very grateful towards Anders Lundbladh and Richard Avellán at GKN Aerospace for their continuing advice and feedback in all areas related to aerospace. Their encyclopedic knowledge and their ability to switch from rigorous analysis to back-of-the-napkin calculations never ceases to amaze me.

To my present and past colleagues at Chalmers, thanks for creating a fun and inspiring working environment. Special thanks to my former roomie Marcus Lejon for being a very good friend and colleague. I always enjoyed our talks, whether it was about compressors, propellers, or if something can be made into a smoothie or not. Thanks to my previous colleagues Basti, Martin, and Oskar for introducing and guiding me at the department when I started as a PhD student. A special thanks to Isak, for being so fun to work with and for always being there when something needed to be designed or built, to Gonzalo whose help has been instrumental in being able to do optimizations, to Daniel for his can-do attitude, and to Carlos for teaching me the secrets of getting papers accepted to journals.

Finally, I would like to thank my family and friends for their enduring support and belief in me, I would not have gotten anywhere without them. For my wonderful wife Charlotta, thank you for picking up my pieces when I hit the wall. A special heart-felt thank you to my mother for teaching me perseverance, and to my father who introduced me to Vetenskapens Värld on Monday evenings. Without them I would not be a scientist today.

This research was funded by the Swedish National Aviation Engineering Research Programme, NFFP. The author would like to acknowledge the financial support of VINNOVA, the Swedish Defence Material Administration (FMV) and GKN Aerospace. Additionally, the author would like to extend his gratitude to the Chalmers Centre for Computational Science and Engineering (C3SE), Gothenburg, Sweden, for providing support and the necessary computational infrastructure for the research.

The future belongs to those who believe in the beauty of their dreams.

- Eleanor Roosevelt

A propeller is really just a big fan to keep the pilot cool. When it stops you can actually see the pilot start sweating.

- the Internet

Nomenclature

Roman upper case letters

A_p	Propeller disk area $[m^2]$
A_{WT}	Wind tunnel cross-sectional area $[m^2]$
B	Number of blades
C_P	Coefficient of power
C_T	Coefficient of thrust
D	Diameter $[m]$
F_j	Flux vector of the transport equations
F_x	Thrust $[N]$
F'_x	Sectional thrust $[N/m]$
H	Source term vector of the transport equations
J	Advance ratio
K	Dimensionality of the design space
N_{cells}	Number of cells in the mesh
N_{DP}	Number of known data points in the RBF
$N_{samples}$	Number of samples for the LHS
P_i	Stacking line control point i
P_k	Turbulent production term
P_{shaft}	Shaft power $[W]$
Pr_t	Turbulent Prandtl number
Q	State vector of the transport equations
Q^0	State vector of previous time step
R	Tip radius $[m]$
T	Static Temperature $[K]$
T_∞	Freestream static temperature $[K]$
U_i	Circumferentially averaged velocity component $[m/s]$
V_∞	Freestream velocity $[m/s]$
$\dot{W}$	Work done by the propeller on the fluid per unit time $[W]$
V_{up}	Measured velocity in wind tunnel $[m/s]$

Roman lower case letters

$b(r_j)$	Basis for the RBF
c	Chord $[m]$
c_{ld}	Design lift coefficient for the NACA16 airfoil profile
d_i	Passage distance parameter for stacking line control point i
$\hat{e}$	Internal energy $[J/kg]$
f	Response surface value
h	Static specific enthalpy $[J/kg]$
h_0	Total specific enthalpy $[J/kg]$
k	Turbulent kinetic energy $[J/kg]$

$\dot{m}$	Mass flow $[kg/s]$
n	Revolutions per second $[1/s]$
p	Static pressure $[Pa]$
r	Radial coordinate $[m]$
r_j	Euclidean distance between two known data points in the RBF
s	Entropy $[J/(kgK)]$
t	NACA16 airfoil profile thickness $[m]$
u_i	Velocity component i $[m/s]$
v_i	Perturbation velocity component $[m/s]$
w_j	RBF weights
y^+	Dimensionless wall distance
y_{wall}	Wall distance $[m]$

Greek letters

χ_i	Design variable i
δ_{ij}	Kronecker delta
ϵ	Turbulence dissipation rate $[m^2/s^3]$
ε	RBF tuning parameter
η	Propeller efficiency (sporadically written as η_{prop})
κ_i	Displacement angle [°] for stacking line control point P_i
κ_r	Displacement angle distribution [°]
μ	Dynamic viscosity $[Ns/m^2]$
μ_t	Eddy viscosity $[Ns/m^2]$
ν	Specific volume $[m^3/kg]$
ω	Turbulence frequency $[1/s]$
ϕ_p	Pressure work $[J/kg]$
ϕ_s	Entropy lost work $[J/kg]$
ρ	Density $[kg/m^3]$
τ_{ij}	Stress tensor $[Pa]$
θ	Azimuthal angle
ξ	Normalized radial position

Subscripts

1	Inlet conditions
2	Wake Analysis plane conditions
FR	Front rotor
n	Normal direction on plane
∞	Freestream conditions
r	Radial direction
RR	Rear rotor
x	Axial direction
θ	Tangential direction

Abbreviations

AF	Activity Factor
BEM	Blade-Element Momentum theory
BPOR	**B**ox**p**rop **O**pen **R**otor
C3SE	Chalmers Centre for Computational Science and Engineering
CAD	Computer-Aided Design
CFD	Computational Fluid Dynamics
CORSIA	Carbon Offsetting and Reduction Scheme for International Aviation
CROR	Counter-Rotating Open Rotor
EBM	Electron Beam Melting
FR	Frozen Rotor interface
FW-H	Ffowcs Williams - Hawkings acoustic analogy
GA	Genetic algorithm
HTR	Hub-to-Tip Ratio
ICAO	International Civil Aviation Organization
ISA	International Standard Atmosphere
LB	Leading Blade
LE	Leading Edge
LHS	Latin Hypercube Sampling
OF	Objective Function
RBF	Radial Basis Function
RF	Radiative Forcing
RPK	Revenue Passenger Kilometers
SLM	Selective Laser Melting
SST	Shear Stress Transport
TB	Trailing Blade
TE	Trailing Edge
WAM	Wake Analysis Method

Contents

1 Introduction

1.1 Aviation and the environment

A major focus of the R&D activities of universities and transport industries in the world regards the reduction of fuel consumption. The major benefits lie in decreased cost, lower greenhouse gas emissions, and improved public health. The challenge of more fuel-efficient transportation is one shared across several major modes of transport, including automotive, naval, and aviation.

In aviation, the amount of passengers is estimated to have reached 4 billion yearly passengers in 2016, and is expected to reach an astounding 7.8 billion by 2036 [1]. Similarly, the International Civil Aviation Organization (ICAO) is projecting that global levels of passenger aviation will increase by 4.6% per year, yielding a 2.5 factor increase in Revenue Passenger Kilometers (RPK) between the year 2012 and 2032 [2]. In this particular industry, fuel has always been a considerable contributor to the costs of operating aircraft, accounting for 29% of all airline costs in 2015 [3] and 19% in 2016 [4].

With regards to the environment the major effect from aviation stems from the emission of greenhouse gases. In contrast to road vehicles or ships where CO_2 emissions play the dominant role in contributing to global warming, aircraft also emit NO_x, water vapour, and soot particles, which at flight altitude leads to increased global temperatures. Additionally, aircraft can produce persistent contrails and clouds, which also contribute to increased global temperatures [5]. Adding these effects together, it reveals that aviation represents 4.9% of the total anthropogenic radiative forcing (RF) [6], which is a measure for the net radiative (heat) imbalance of Earth's climate system caused by human activities.

With the current level and projected growth of air travel in mind there is a great need for technological, operational, and infrastructure measures which decrease fuel consumption and emissions. This is also mentioned in the proposed Carbon Offsetting and Reduction Scheme for International Aviation (CORSIA) agreement [7], which outlines how the aviation industry needs to change on a global level for improved environmental sustainability. This agreement not only calls for more efficient aircraft, but also improved operations, increased use of bio-fuels, better route planning, and proposes a global scheme for carbon trading and offsetting. Better route planning in terms of staging [8] and contrail-avoidance [9, 10] have also been suggested for decreasing radiative forcing from aviation.

Entirely new types of aircraft have been suggested for decreased fuel consumption and emissions by employing electrification, bio-fuels, high aspect-ratio wings, and boundary layer ingestion [11, 12]. According to NASA decreases in fuel consumption of 50-70% could be realized by incorporating these technologies together with lower cruise speeds and more efficient engines.

Aero engines will have to play its part by introducing new innovative technologies and concepts. These new technologies can include new heat recuperation concepts, unconventional combustion technologies, and novel propulsive systems [13]. More integrated powerplant and aircraft configurations may also pave a way forward, as being demonstrated by the NASA X-57 Maxwell [14] which incorporates distributed electric propulsion.

Figure 1.1.1: *Illustration of a pusher-type Counter-Rotating Open Rotor (CROR) concept using Boxprop blades on the front rotor. Flow from left to right.*

1.2 The Counter-Rotating Open Rotor

Counter-Rotating Open Rotors (CROR) are part of the aforementioned aero engine technologies and could potentially offer double-digit fuel savings compared to turbofans. Compared to geared turbofans with year 2020 technology level the CROR is estimated to have a 15% lower fuel consumption [15]. The fuel savings are realized by employing two rows of large-diameter, counter-rotating propeller blades as shown in Fig. 1.1.1, which result in a higher bypass ratio than existing turbofan engines, thereby increasing propulsive efficiency. Another major aerodynamic benefit for the CROR is the lack of an outer nacelle surrounding the propeller blades, which decreases aerodynamic drag and weight compared to a turbofan.

CROR engines were researched extensively in the US in the 1970s and 1980s due to the energy crisis of 1973, and the research programs incorporated design and testing of several CROR designs (in the US often called propfans or unducted fans) [16]. This effort culminated in test flights of the GE Unducted Fan (UDF) demonstrator installed on a McDonnell Douglas MD-80 and a trans-Atlantic flight to the Farnborough International Airshow in 1988 [17]. Fuel savings of 25-30% were achieved compared to equivalent turbofan engines of the time [16], but it had trouble complying with the noise requirements outlined in ICAO Chapter 3 [18]. In the end, technological and economical risk, noise levels, public acceptance, and the fact that fuel prices declined led to a decreased commercial interest in the CROR.

As mentioned earlier, the lack of an outer nacelle for the CROR decreases drag but it also removes the ability to shield the surroundings from the noise produced by the propeller blades. This noise is not only due to the rotation of the blades but also due to the tip vortices and wakes from the front propeller blades impinging on the rear

propeller blades. The level of this type of noise, also called interaction noise, is most critical during take-off conditions due to the high loading of the blades, leading to high angles-of-attack, strong tip vortices, and often separated flow [19, 20]. Several measures have been suggested for decreasing the noise levels. A common approach is where the rear blade of a CROR is clipped in order for the tip vortex of the front rotor to flow past it without impinging on it. Unfortunately, this measure also increases the power loading of the rear rotor and decreases its efficiency. The blade counts of the forward and rear rotor also have impact on noise, and from an acoustic point of view it would be preferable to have unequal number of front and rear blades without a common denominator [21–23]. Aeroacoustic optimization of the blade shapes is also a possibility for decreasing noise levels, as has been demonstrated by Schnell [23] and Lepot [24], as is using serrated trailing edges [25]. A simple, yet effective approach for decreasing noise and improving efficiency at take-off conditions was demonstrated by Zachariadis [19], which involved increasing the rotational speed of the front rotor of the CROR and re-pitching it, leading to lower angles-of-attack, smaller separation bubbles, decreased front rotor tip vortex strength, and therefore lower noise. Other interesting approaches for decreasing tip vortex strength are shown in Fig. 1.2.1 and include propeller blades with winglets as was presented by General Electric [26], incorporating a small nozzle at the tip of the blade for disrupting the tip vortex by Rolls Royce [27], and special shaping of the blade to produce a leading edge vortex which counteracts the tip vortex as suggested by Snecma [28].

These advances notwithstanding, the noise level of the CROR is one of several hurdles in the path to its commercial adaptation, and the noise levels need to be decreased below current and future ICAO noise standards in order for the CROR to be widely adapted in the aviation industry, especially considering the long development times in aviation for fielding radically new technologies.

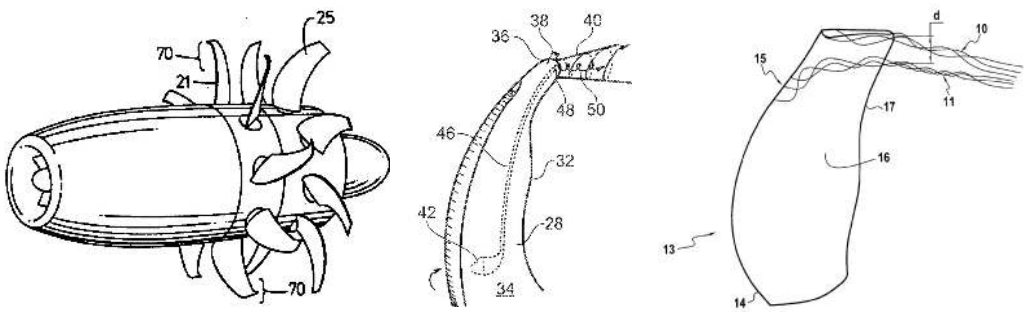

Figure 1.2.1: *Different proposed measures for decreasing tip vortex strength of open rotor blades. Propeller blades* ***(a)*** *equipped with winglets,* ***(b)*** *equipped with a nozzle at the tip which disrupts the tip vortex, and* ***(c)*** *designed to produce a leading edge vortex to counteract the tip vortex.*

1.3 The Boxprop

The Boxprop concept was conceived by Richard Avellán and Anders Lundbladh in 2009 [29] as an idea for a propeller blade with reduced tip vortex strength compared to conventional blades. As can be seen in Fig. 1.3.1, the Boxprop consists of pair-wise tip-joined blades, whose blade halves are denoted *Leading Blade (LB)* and *Trailing blade (TB)* with respect to the rotational direction. The Boxprop is conceptually similar to a box wing, and can potentially reduce tip vortex strength, leading to higher efficiency, lower interaction noise, and incorporate higher structural rigidity. If the Boxprop is used as a front rotor of a CROR as suggested in Fig. 1.1.1, then the increased rigidity might allow for forward sweeping of the front rotor blades, increasing the distance between it and the rear counter-rotating rotor. This increased distance would allow more mixing of the tip vortices and wakes, which is also beneficial from a noise perspective.

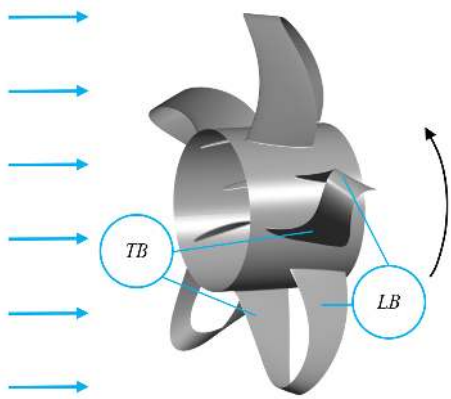

Figure 1.3.1: *Boxprop blade notation, direction of rotation and inflow direction.*

1.4 Purpose

The purpose of the work presented in this thesis has been to investigate if the Boxprop can operate in a CROR without generating a tip vortex and consequently operate with lower noise levels while remaining aerodynamically competitive with conventional propeller blades. In order accomplish this the following questions need to be answered:

- How should a Boxprop be designed for maximum efficiency?
- How well does the Boxprop perform compared to conventional propeller blades?
- Can the Boxprop operate without producing a tip vortex?
- How can the Boxprop be integrated into a CROR?
- At take-off conditions, does a CROR equipped with a Boxprop generate less noise?

2 Design Procedure

This chapter will cover the definition of common propeller performance parameters, the Boxprop design approach and geometric parametrization, conventional propeller design, and how a CROR can be designed with a Boxprop as the front rotor and a conventional propeller as the rear rotor.

2.1 Propeller performance parameters

Propeller performance is typically specified in terms of non-dimensional numbers. These include the advance ratio J, power coefficient C_P, thrust coefficient C_T, and propeller efficiency η, as defined in Eq. 2.1.1 to 2.1.4.

$$J = \frac{V_\infty}{nD} \tag{2.1.1}$$

$$C_P = \frac{P_{shaft}}{\rho_\infty n^3 D^5} \tag{2.1.2}$$

$$C_T = \frac{F_x}{\rho_\infty n^2 D^4} \tag{2.1.3}$$

$$\eta = \frac{F_x V_\infty}{P_{shaft}} \tag{2.1.4}$$

The *Activity Factor AF* is a measure of the propeller area, and a larger AF results in a propeller that can absorb more power:

$$AF = \frac{10^5}{16} \int_{\xi_{hub}}^{\xi_{tip}} \left(\frac{c}{D}\right) \xi^3 d\xi \tag{2.1.5}$$

The chord is weighted by the non-dimensional radius $\xi = r/R$ cubed, meaning that a propeller with a specific chord value at the tip can input more power than one with the same chord near the hub.

2.2 Boxprop design

2.2.1 Development of the Boxprop design approach

Early Boxprop research which led to Paper I and II utilized an in-house code named BBCode, which is extensively documented in the theses by Adriansson [30] and by Olofsson & Pettersson [31]. The code constructs an arc-shaped stacking line, and stacks airfoil sections along its length. The airfoil sections are of the NACA 16 type [32], and pre-defined distributions of chord, thickness, camber, and angle-of-attack are used to

construct and properly position the airfoils on any given position along the stacking line. The points of the airfoil sections are then exported into CAD-software such as Autodesk Inventor or Dassualt CATIA, where the points are used to create splines, which in turn are used to construct lofted surfaces. These surfaces were then exported into `.step` CAD files, which were read and meshed using ANSYS Meshing. This process was satisfactory for simulating a handful of cases, but is unsuitable for larger systematic studies which require the simulation of hundreds of designs since it is both time-intensive and involves a high degree of manual input, which leads to high turnaround times for simulating new designs.

In Paper III a new design approach for the Boxprop was presented which coupled stochastic optimization and CFD. This approach was chosen since existing propeller designs methods such as the Blade Element Momentum (BEM) [33], Vortex [34], and lifting line methods [21] were falling short for the aerodynamic design of the Boxprop. CFD simulations of early Boxprop geometries included in Paper I and II showed that different distributions of camber and angle-of-attack were required for each blade half because of their mutual interference - a factor which cannot be accounted for by using BEM/Vortex methods. The interference could possibly have been accounted for using lifting line methods, which can predict the mutually induced flow due to the presence of the blades, but the flow around the Boxprop is transonic and can feature shocks in the blade passage, thereby invalidating the use of these methods which have otherwise been used successfully for the design of conventional open rotor blades [21]. As a consequence, the chosen path for finding aerodynamically optimal Boxprop designs was to employ the use of 3D CFD together with an evolutionary algorithm, an approach which has been previously used in Chalmers for the aerodynamic optimization of axial compressors [35–37]. The resulting optimal designs can then be analyzed using the Wake Analysis Method derived in Chapter 5 of this thesis for increased understanding of the magnitude of the aerodynamic losses.

2.2.2 Boxprop parametrization

The design variables of the Boxprop parametrization are divided into two main categories; variables which are used to construct the blade **stacking line**, and variables that are used to set airfoil **sectional properties** such as camber, chord, and angle-of-attack relative to the undisturbed flow.

The **blade stacking line** is composed of two Bézier curves, one for each blade half, as is illustrated in Fig. 2.2.1. The Beziér curve for each blade half is constructed using control points P_i, which in turn are defined using a blade passage distance d_i and a chord displacement angle κ_i. These parameters essentially control the amount of sweep on the LB and TB and define together with the radial positions for P_1 (hub radius, fixed), P_2 (set as an optimization variable), and P_4 (tip radius, fixed) the stacking line Bézier curves. The control point P_3 has a z-coordinate equal to the tip radius in order to obtain tangency between the stacking lines of each blade half. Using this approach, the LB and TB become mirror-symmetric, which enables each blade half to be swept in opposite directions, while providing a balanced mechanical layout whose center-of-gravity lies close to the z-axis of the rotor.

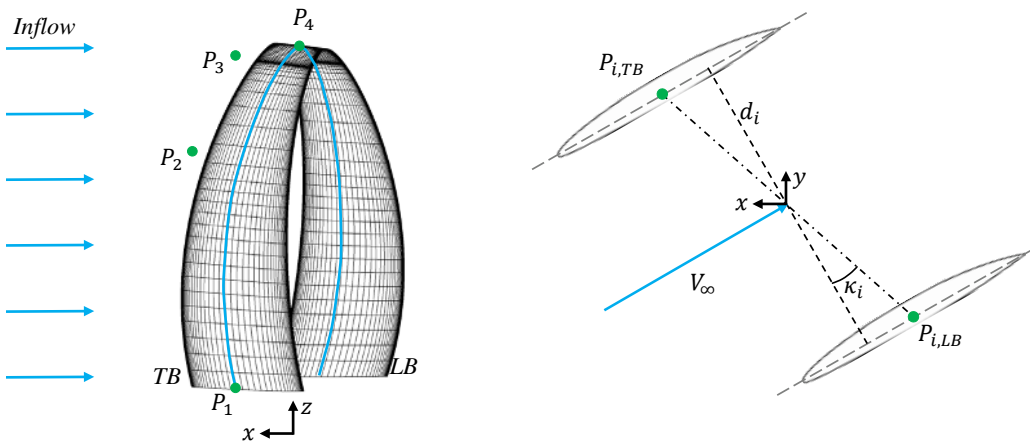

Figure 2.2.1: *Stacking line parametrization. The blade passage distance d_i is defined as perpendicular to the local undisturbed flow vector V_∞.*

The **sectional properties** of the propeller are also defined as radial distributions by means of Bézier curves, whose control points are used as design parameters for the optimization, exemplified in Fig. 2.2.2 for camber by using a quartic Bézier curve. Once the sectional properties camber, chord, and angle-of-attack are set, NACA16 airfoil profiles [32] are constructed, positioned on planes normal to the stacking line, and rotated to meet the undisturbed flow at the specified angle-of-attack. For the optimizations included in this thesis, computational cost has been reduced by setting a fixed airfoil section thickness-to-chord ratio t/c distribution identical to the one used by the NASA SR7L propeller [38]. The SR7L high speed propeller also employed NACA16 airfoil sections and operated at similar transonic flow conditions. The abundance in design data pertaining to the SR7L made it a suitable source of information for setting up ranges for thickness, chord, and camber distributions, especially since this propeller was ultimately manufactured and tested in a wind tunnel at transonic conditions.

2.3 Conventional propeller design

2.3.1 Initial design

Conventional propellers are very useful as a basis of comparison for the Boxprop in terms of aerodynamic performance and loss composition. Relatively early in the research project it was found that there was a need for a propeller design code for the initial design of minimum-induced loss propellers. The development of the in-house propeller design code OPTOPROP is reported in detail in Paper VIII - *Implementation of Blade Element Momentum/Vortex Methods for the Design of Aero Engine Propellers* - and will be very briefly recapped here.

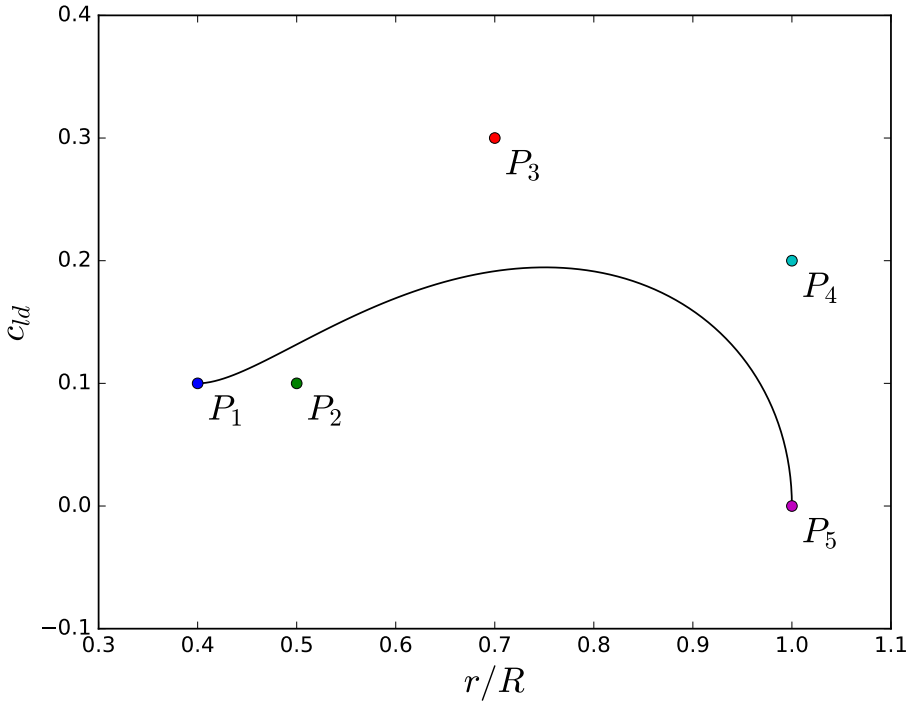

Figure 2.2.2: *An example of a quartic (fourth order) Bézier curve for the definition of the camber distribution c_{ld}. The same type of curve is used for the definition of the chord and angle-of-attack distributions.*

Propeller design and analysis methods range in complexity from the analytical Actuator Disk method (also called momentum theory) [39] which only treats the propeller as a infinitely thin disk where the flow experiences a discontinuous pressure increase. The more complex Blade Element Theory [39] is useful for calculating the forces on a blade element given the oncoming flow. Unfortunately, it is unable to account for the effect of the blade on the flow, and therefore neglects the flow induced by the propeller. Joining the two theories together one obtains the Blade Element-Momentum theory (BEM), which connects the thrust and torque on the blade with the change in linear and angular momentum in the flow. Another variant is combining the Blade Element method with a vortex model for the wake by relating the circulation in the blade sections to the circulation (swirl velocity) in the wake downstream of the propeller [33, 34, 39, 40]. Beyond these methods there are also numerical design methods with increasing complexity based on the lifting line [41, 42] and lifting surface methods [43].

The design methods implemented in OPTOPROP are the ones by Larrabee [40], Adkins [33], and Drela [34] and are of the Blade Element-Vortex type, striking a balance in method complexity and capability. The three methods are compared to results from

experiments and CFD simulations, yielding good accordance in the trends of performance values such as propeller efficiency and thrust. The methodology by Drela is found to be quite capable, even taking into consideration the case of non-uniform inflow to the propeller, making it an ideal choice for the design of the rear propeller in a CROR.

2.3.2 Conventional propeller parametrization for optimization

The initial propeller designs obtained with OPTOPROP are most suitable as baseline designs for further aerodynamic optimization. The conventional propellers employ a parametrization based on Bézier curves similar to the one described for the Boxprop in Chapter 2.2.2, but instead of representing the actual values of chord, camber, blade angle, and stacking line coordinates they represent differences from the baseline design. The conventional blades included in the papers of this thesis also use the profile thickness distribution from the SR7L propeller, just like the Boxprop.

2.4 CROR design

The design process of a CROR featuring a Boxprop front rotor and a rear conventional propeller can be summarized as follows:

1. First, a simplified CROR design is created with pre-set design properties such as diameter, blade counts, intra-rotor spacing, blade clipping, operating point, and other important geometric properties. Additionally, target torque split, required thrust level, and assumed propeller efficiencies based on experience and literature are set. In this step it is important to compare the target thrust and the assumed propeller efficiency of the Boxprop with existing optimization databases in order to obtain a sensible estimate.

2. A Boxprop capable of delivering the required thrust is chosen from an existing optimization or propeller database. It is then simulated, its performance checked, and the velocity profiles for the axial and swirl velocities are extracted at a downstream location corresponding to where the rear rotor would be located.

3. The velocity profiles are used as input for the in-house propeller design tool OPTOPROP. A conventional propeller design is generated for a pre-specified thrust coefficient, and a preliminary estimate of the propeller efficiency is obtained.

4. The front Boxprop and the rear conventional propeller are used to synthesize a CROR, which is then meshed, simulated with ANSYS CFX, and post-processed.

The obtained design can also be aerodynamically optimized by employing the optimization framework presented in Chapter 4.

3 CFD Methodology

The CFD modeling mentioned in this thesis covers two main cases of simulations, namely optimization and more detailed aerodynamic and wake analyses. The governing equations and turbulence modelling are identical for both, but domain sizes and mesh cell counts differ.

3.1 Governing equations

For the steady-state simulations presented in this thesis the solver ANSYS CFX has been used. The time-averaged equations for mass, momentum, and energy are solved together with the transport equations of the $k-\omega$ SST turbulence model. These are outlined below in compact form:

$$\frac{\partial \mathcal{Q}}{\partial t} + \frac{\partial \mathcal{F}_j}{\partial x_j} = \mathcal{H} \tag{3.1.1}$$

The state vector $\mathcal{Q}$ corresponds to:

$$\mathcal{Q} = \begin{bmatrix} \bar{\rho} \\ \bar{\rho}\tilde{u}_i \\ \bar{\rho}\tilde{h}_0 - \bar{p} \\ \bar{\rho}\tilde{k} \\ \bar{\rho}\tilde{\omega} \end{bmatrix} \tag{3.1.2}$$

Here the flow variables ψ have been decomposed using either the Reynolds decomposition $\psi = \bar{\psi} + \psi'$, or the Favre decomposition $\psi = \tilde{\psi} + \psi''$. The flux vector $\mathcal{F}_j$ in Eq. 3.1.1 is defined as:

$$\mathcal{F}_j = \begin{bmatrix} \bar{\rho}\tilde{u}_j \\ \bar{\rho}\tilde{u}_j\tilde{u}_i + \bar{p}\delta_{ij} - \tau_{ij} \\ \bar{\rho}\tilde{u}_j\tilde{h}_0 - \lambda\frac{\partial \tilde{T}}{\partial x_j} - \frac{\mu_t}{Pr_t}\frac{\partial \tilde{h}}{\partial x_j} - \tilde{u}_i\tau_{ij} \\ \bar{\rho}\tilde{u}_j k - \left(\mu + \frac{\mu_t}{\sigma_{k3}}\right)\frac{\partial k}{\partial x_j} \\ \bar{\rho}\tilde{u}_j\omega - \left(\mu + \frac{\mu_t}{\sigma_{\omega 3}}\right)\frac{\partial \omega}{\partial x_j} \end{bmatrix} \tag{3.1.3}$$

The source term vector $\mathcal{H}$ of Eq. 3.1.1 contains the sink and source terms of the transport equations for k and ω:

$$\mathcal{H}_j = \begin{bmatrix} 0 \\ 0 \\ 0 \\ P_k + \beta'\rho k\omega \\ 2\rho\frac{1-F_1}{\sigma_{\omega 2}\omega}\frac{\partial k}{\partial x_j}\frac{\partial \omega}{\partial x_j} + P_k\alpha_3\frac{\omega}{k} - \rho\omega^2\beta_3 \end{bmatrix} \tag{3.1.4}$$

The working fluid is treated as a thermally perfect gas and as a Newtonian fluid. The turbulent stresses that arise when employing the Reynolds decomposition mentioned earlier give rise to turbulent stresses, which are modelled using the Boussinesq assumption, resulting in a stress tensor τ_{ij} as shown below in Eq. 3.1.5.

$$\tau_{ij} = (\mu + \mu_t)\left(2\tilde{S}_{ij} - \frac{2}{3}\tilde{S}_{kk}\delta_{ij}\right) - \frac{2}{3}\delta_{ij}\rho k \tag{3.1.5}$$

The strain rate tensor $\tilde{S}_{ij}$ and the eddy viscosity μ_t is calculated as shown below:

$$\tilde{S}_{ij} = \frac{1}{2}\left(\frac{\partial \tilde{u}_i}{\partial x_j} + \frac{\partial \tilde{u}_j}{\partial x_i}\right) \tag{3.1.6}$$

$$\mu_t = \rho \frac{\sqrt{C_\mu}k}{max(\sqrt{C_\mu}\omega, (\bar{S}_{ij}\bar{S}_{ij})^{0.5}F_2)} \tag{3.1.7}$$

Now that the eddy viscosity is known, the turbulence production term P_k can be calculated. In CFX, this is done using the following equation:

$$P_k = \frac{\partial \tilde{u}_i}{\partial x_j}\left(\mu_t\left(2\tilde{S}_{ij} - 2\tilde{S}_{kk}\delta_{ij}\right) - \frac{2}{3}\delta_{ij}\rho k\right) \tag{3.1.8}$$

The $k-\omega$ SST turbulence model is a blend between a $k-\epsilon$ and a $k-\omega$ turbulence model that switches between the two models depending on the distance from the nearest wall. A blending function F_1 (see Eq. 3.1.9) is used, which is equal to one near the wall and zero outside of the boundary layer, resulting in a $k-\omega$ turbulence model at the wall, and a $k-\epsilon$ model elsewhere. The reason for this is that the $k-\omega$ is known to perform better than the $k-\epsilon$ near the wall and vice-versa [44].

$$F_1 = tanh(a_1^4) \tag{3.1.9}$$

$$a_1 = min\left[max\left(\frac{\sqrt{k}}{\beta'\omega y_{wall}}, \frac{500y_{wall}}{y_{wall}^2\omega}\right), \frac{4\rho k}{\mathcal{C}_{kw}\sigma_{\omega 2}y_{wall}^2}\right] \tag{3.1.10}$$

$$\mathcal{C}_{kw} = max\left[2\rho\frac{1}{\sigma_{\omega 2}\omega}\frac{\partial k}{\partial x_j}\frac{\partial \omega}{x_j}, 10^{-10}\right] \tag{3.1.11}$$

For the turbulent viscosity (Eq. 3.1.7) another blending function F_2 is needed, and its definition is shown in Eq. 3.1.12.

$$F_2 = tanh(a_2^2) \tag{3.1.12}$$

$$a_2 = max\left(\frac{2\sqrt{k}}{\beta'\omega y_{wall}}, \frac{500y_{wall}}{y_{wall}^2\omega}\right) \tag{3.1.13}$$

The model constants required for the turbulence transport equations can be divided into two types; the first type is a regular constant while the second type is a linear combination of the constants from the underlying $k-\epsilon$ and a $k-\omega$ turbulence models using the

blending function F_1. The second type is denoted by the subscript $_3$ (e.g. σ_{k3}), and is calculated as in Eq. 3.1.14.

$$\mathcal{C}_3 = F_1\mathcal{C}_{k-\omega} + (1 - F_1)\mathcal{C}_{k-\epsilon} \tag{3.1.14}$$

The remaining constants required for establishing Eq. 3.1.1 to Eq. 3.1.12:

$$[\alpha_1,\, \alpha_2,\, \beta_1,\, \beta_2,\, \beta',\, C_\mu, \sigma_{\omega 2},\, Pr_t] = [5/9,\, 0.44,\, 0.075,\, 0.0828,\, 0.09,\, 0.09,\, 1.168,\, 0.9]$$

3.2 Discretization

In ANSYS CFX discretization is carried out by constructing a control volume around each mesh node, and integrating the governing equations (Eq. 3.1.1) over the volume $\mathcal{V}$ surrounding the node. Assuming that the control volume does not deform in time and employing Gauss' theorem on the flux vector $\mathcal{F}_j$, the following equation is obtained:

$$\frac{\partial}{\partial t}\int_{\mathcal{V}} \mathcal{Q} d\mathcal{V} + \int_S \mathcal{F}_j n_j dS = \int_{\mathcal{V}} \mathcal{H} d\mathcal{V} \tag{3.2.1}$$

The discretization of the transient term is done using a temporal discretization scheme. In this thesis a first order Backward Euler scheme has been used:

$$\frac{\partial}{\partial t}\int_{\mathcal{V}} \mathcal{Q} d\mathcal{V} \approx \mathcal{V}\left(\frac{\mathcal{Q} - \mathcal{Q}^0}{\Delta t}\right) \tag{3.2.2}$$

Here the superscript ^{0} denotes the previous timestep. The flux vector $\mathcal{F}_j$ includes both advective and diffusive terms, and these are treated differently from each other. The advective terms are discretized using a second order accurate upwind scheme, named *High Resolution Scheme* by CFX. The gradients needed to calculate the diffusive terms included in the flux vector $\mathcal{F}_j$ are evaluated using finite-element shape functions. In ANSYS CFX, the values of the flow variables are stored at the mesh nodes, and if a variable value or gradient is needed, it is computed using finite-element shape functions for any position inside the control volume around each node. More details on the discretization and the solution strategy of ANSYS CFX can be found in the CFX Solver Theory Guide [45].

3.3 Domain setup

The domain types used in this thesis are illustrated in Fig 3.3.1 and 3.3.2. The majority of the simulations presented concern either aerodynamic optimization or wake analysis of high speed propellers, and the domain layouts reflect this. Both domain types encompass an inner 3D domain representing one blade passage and outer quasi-2D domain. Additionally, the 3D domain is solved in the rotating reference frame. The domain setup used in this work allows the pressure field around the propeller to propagate outwards towards the freestream while maintaining a low overall cell count. The following boundary conditions and interfaces are used:

- Inlet - Specified with total pressure, total temperature, flow direction and turbulence intensity. These values are obtained using the flight Mach number, altitude, and tables representing the International Standard Atmosphere (ISA).
- Opening - Defined as the CFX equivalent of a freestream boundary condition (opening/entrainment) with a specified static pressure boundary condition. The boundary condition for turbulence is set as zero-gradient.
- Outlet - Static pressure is set equal to the International Standard Atmosphere (ISA) for a given flight altitude.
- Hub - Set as a free slip wall. Modelling of the nacelle boundary layer was omitted for optimization and wake analysis cases since it would add additional design parameters with a limited influence on propeller performance. Paper VI includes a comparison between cases ran with no slip and free slip hubs and showed differences in thrust of 2% and propeller efficiency of 0.76% for the Boxprop. For the analyzed conventional propeller the differences amount to 1.27% in thrust and 0.17% in propeller efficiency for the conventional blade.
- Blade - The boundary condition for the blade surface is set as a no-slip adiabatic wall.
- Frozen Rotor Interfaces - The frame-change capability of these interfaces allow for the steady-state simulation of the outer 2D domain in the stationary reference frame while the 3D domain is simulated in the rotating reference frame.
- Rotational periodic boundary conditions - Only one blade passage is modelled in the 3D domain, and to account for the rest of the rotor periodic boundary conditions are used. The outer 2D domain also employs periodic boundary conditions in order to properly represent the annular volume around the 3D domain.

For the optimization cases a relatively small domain is used to enclose the propeller, thereby decreasing computational cost and making the aerodynamic optimization more affordable in terms of computational resources. A domain and mesh study was included in Paper III in order to find a suitable domain size. For wake analysis, a larger inner 3D domain is used in order to capture the wake development downstream of the propeller.

3.4 Meshing

Initially, both the Boxprops and the conventional propellers were meshed with ANSYS Meshing, which produced tetrahedral meshes everywhere in the 3D domain except at the blade and hub surfaces, whose boundary layers were meshed with triangular prism elements. The mesh sizing normal to blade surfaces was chosen in order to accommodate a low-Reynolds near wall formulation, which was reached by adhering to an average first node height of $y^+ < 2$. This approach resulted in very low turnaround times and yielded sufficient accuracy for performance simulations. The main disadvantage of this approach is a higher amount of cells when compared to a structured hexahedral mesh, and higher

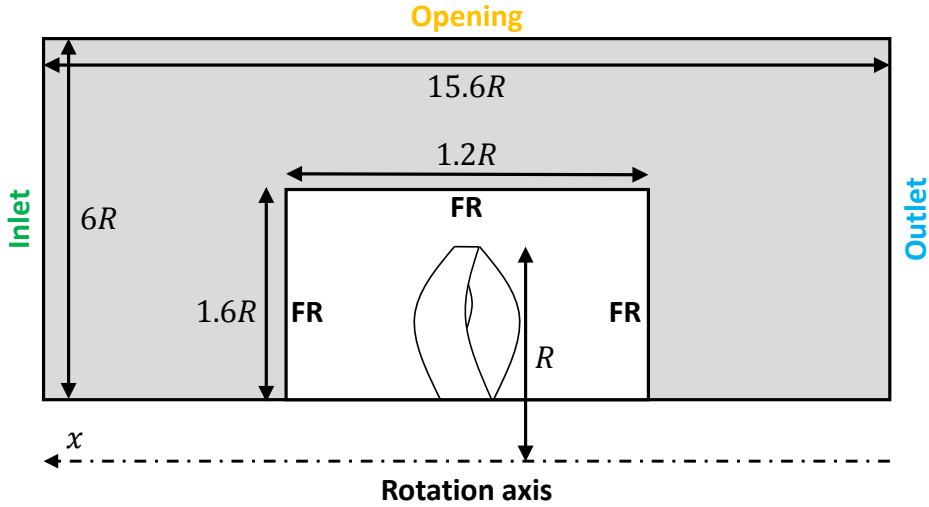

Figure 3.3.1: *Illustration of the domain topology for the optimization cases. The inner 3D domain contains one single rotor passage while the outer 2D domain (grey) accounts for the far-field effects. The position of the inlet, outlet, Frozen Rotor interfaces (FR), and opening boundaries is also shown.*

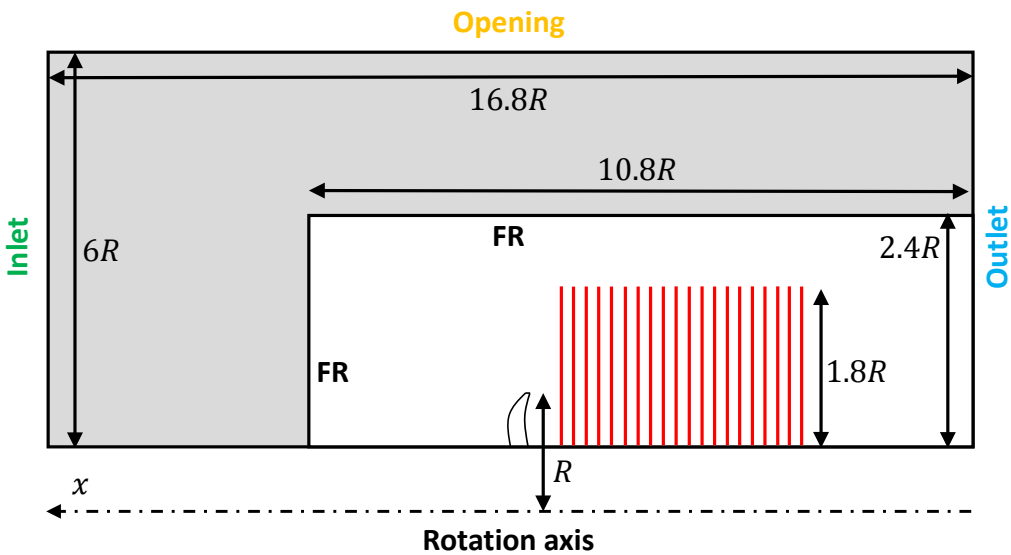

Figure 3.3.2: *Illustration of the domain topology for the wake analysis cases. The inner 3D domain contains one single rotor passage while the outer 2D domain (grey) accounts for the far-field effects. The position of the inlet, outlet, Frozen Rotor interfaces (FR), and opening boundaries is also shown. The red planes exemplify the location and extent of the integration planes used in the Wake Analysis Method.*

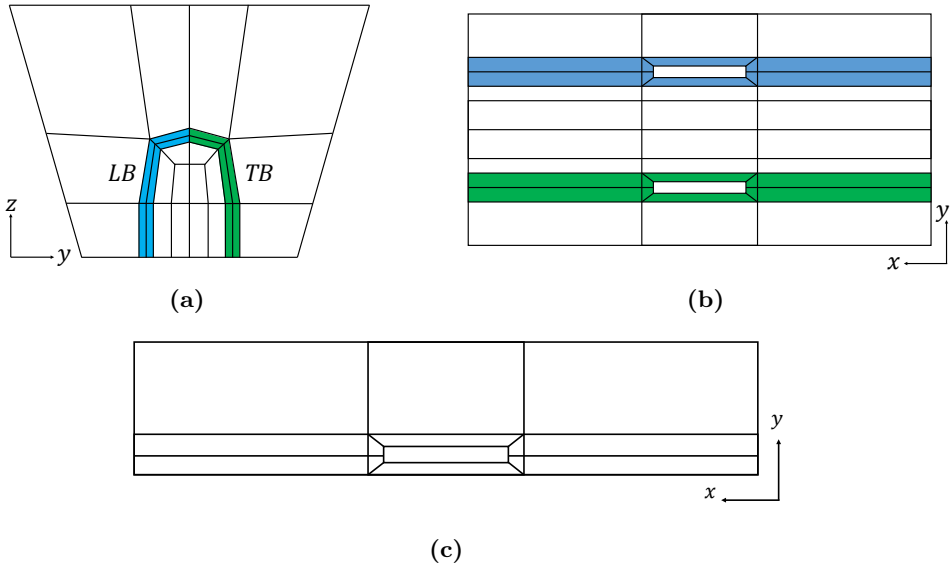

Figure 3.4.1: ***a)*** *and* ***b)*** *Boxprop blocking structure. Blue denotes the wake and O-grid blocks for the LB of the Boxprop, while green is for the TB.* ***c)*** *The conventional propeller blocking structure.*

numerical dissipation of wakes and tip vortices, making this type of simulation slower and making it unsuitable for more detailed aerodynamic analysis. For steady state simulations of the performance of single propellers and even counter-rotating propellers, this type of mesh is adequate, and in the latter case a mixing plane interface is usually added between the two counter-rotating propeller domains, which by definition mixes out the flow properties in the circumferential direction.

Due to the inherent disadvantages in using tetrahedral meshes, it was decided to switch over to structured hexahedral meshes using ANSYS ICEM CFD for both the optimization and the wake analysis cases. Both types of cases share the same fundamental blocking structure, which is shown in Fig. 3.4.1a and 3.4.1b for the Boxprop and in Fig. 3.4.1c for the conventional propellers. The meshes resulting from these blocking structures were used for the optimization cases and are shown in Fig. 3.4.2 and in Fig. 3.5.1 for a 6-bladed Boxprop and a 12-bladed conventional propeller, respectively. It should be noted that the meshes shown here are for the optimization cases, and feature mesh counts in the order of 1 to 2 million cells, and are relatively coarse compared to the meshes used for wake analysis, which commonly feature cell counts between 15 to 50 million cells depending on propeller type and number of blades. The higher cell count is due to the need for properly resolving sharp flow features such as blade wakes and tip vortices for a relatively long downstream distance from the blade. In this work, the mesh is aligned with the helical shape of the undisturbed flow until a downstream distance of approximately $0.5D$ from the blade TE, thereby allowing the refined wake blocks of the mesh to capture the wake velocity profile without too much numerical dissipation.

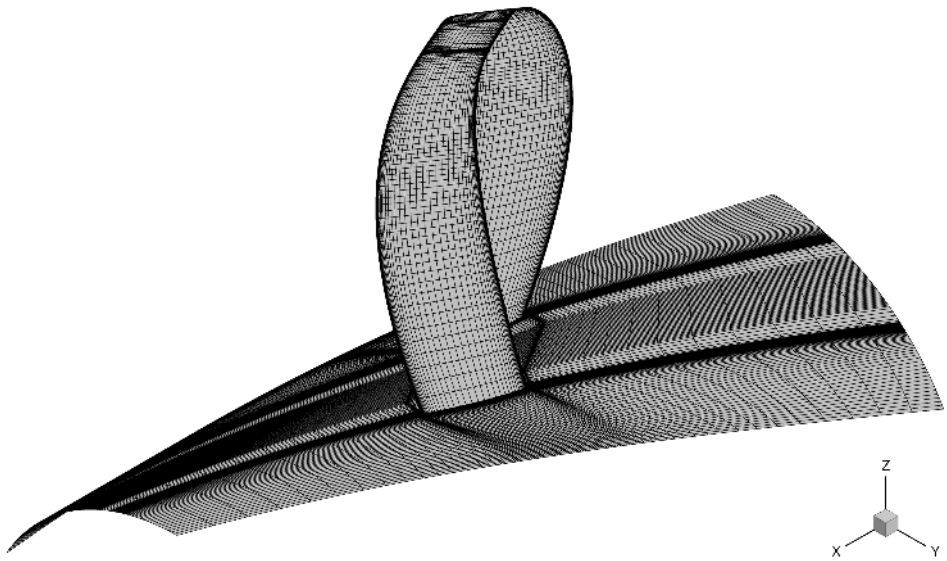

Figure 3.4.2: *Example of a mesh used for the aerodynamic optimization of a 6-bladed Boxprop blade. The mesh featured approximately 1.84 million cells.*

3.5 Mesh study for Boxprop optimization cases

Table 3.5.1: *Mesh study for a 5-bladed Boxprop. All changes are relative to case BP1 (bold). Changes in thrust coefficient C_T are proportional, while the absolute difference is shown for the propeller efficiency η.*

Case	N_{cells} $[10^6]$	ΔC_T	$\Delta\eta$ [%]
BP1	**4.25**	**0%**	**0%**
BP2	2.48	0.35%	0.00%
BP3	1.37	−0.74%	−0.40%
BP4	0.98	−0.71%	−0.49%
BP5	0.74	−1.06%	−0.60%

A mesh study for the Boxprop blades was performed in Paper III for a 5-bladed Boxprop, whose results are shown in Table 3.5.1. As can be seen, the differences in performance values are relatively small for the presented mesh cases, and a mesh size of 1.15 million cells was chosen for Paper III, as a compromise between computational cost and and fidelity. For Paper V and subsequent papers a 6-bladed Boxprop was used instead, and the mesh cell count was increased to 1.84 million cells, in order to better resolve the shocks in the flow. It is assumed that the mesh study for the 5-bladed Boxprop is also valid for the 6-bladed Boxprop since the geometric properties of both propellers such as chord, thickness, and sector size are very similar. An example of a Boxprop mesh used for aerodynamic optimization is shown in Fig. 3.4.2.

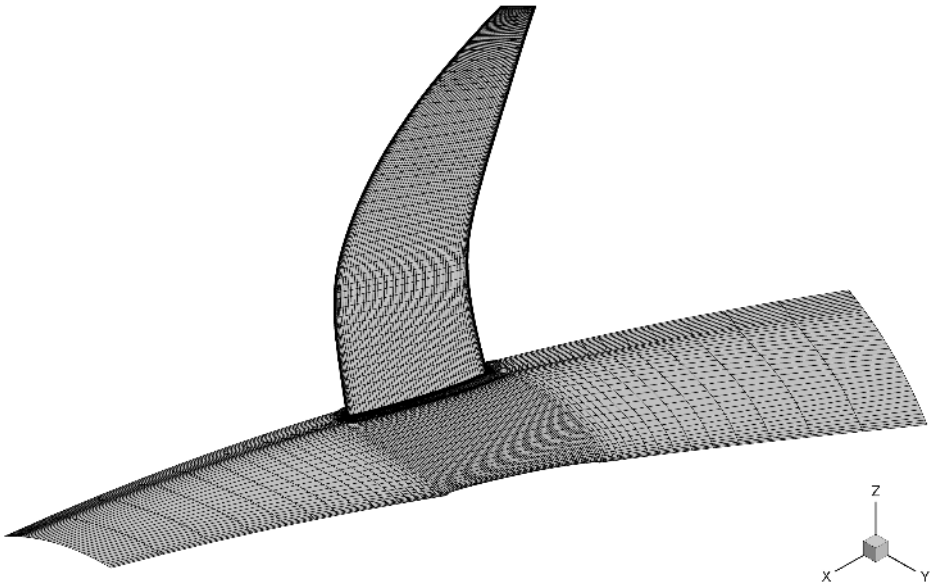

Figure 3.5.1: *Example of a mesh used for the aerodynamic optimization of a 12-bladed conventional propeller blade. The mesh featured approximately 0.82 million cells.*

3.6 Mesh study for conventional blade optimization cases

Paper V includes a mesh study for a 6 and a 12-bladed conventional propeller, and it is shown here in Table 3.6.1 and 3.6.2 in greater detail. As can be seen, the differences in performance are relatively small between the coarsest and finest mesh in this study, and therefore the coarsest meshes were used for the optimization efforts.

Table 3.6.1: *Mesh study for a 6-bladed conventional propeller. All changes are relative to case 6A (bold). Changes in thrust coefficient C_T are proportional, while the absolute difference is shown for the propeller efficiency η.*

Case	N_{cells} $[10^6]$	ΔC_T	$\Delta\eta$ [%]
6A	**3.52**	**0%**	**0%**
6B	2.58	−0.08%	0.00%
6C	1.91	−0.05%	−0.05%
6D	1.39	−0.18%	−0.10%
6E	1.03	−0.72%	−0.12%

Table 3.6.2: *Mesh study for a 12-bladed conventional propeller. All changes are relative to case 12A (bold). Changes in thrust coefficient C_T are proportional, while the absolute difference is shown for the propeller efficiency η.*

Case	N_{cells} $[10^6]$	ΔC_T	$\Delta\eta$ [%]
12A	**2.73**	**0%**	**0%**
12B	2.00	0.01%	−0.01%
12C	1.49	−0.04%	−0.01%
12D	1.10	−0.16%	−0.04%
12E	0.82	−0.25%	−0.11%

4 Optimization Framework

4.1 Structure of the optimization framework

In order to understand which level of aerodynamic performance can be obtained from the Boxprop or any other propeller, optimal designs are needed with as low levels of loss as possible. For this end, an in-house version [46] of the NSGA-II [47] genetic algorithm (GA) was adopted and incorporated into an optimization platform.

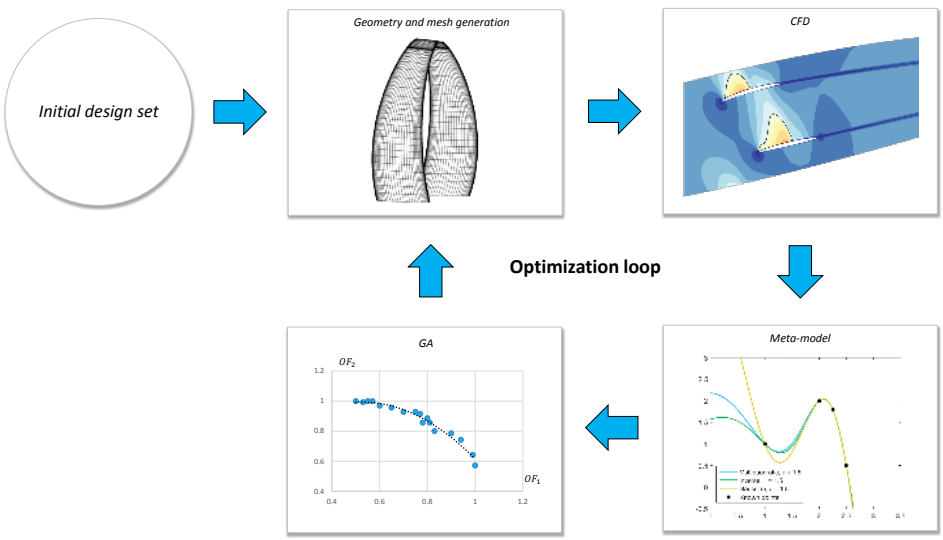

Figure 4.1.1: *Schematic overview of the optimization platform and its constituent components.*

The structure of the multi-objective optimization platform employed in this work is shown in Fig. 4.1.1 and is described in detail in Paper III. The objective functions of the optimization are to maximize the propeller efficiency and thrust coefficient of the propeller for a given operating point. The overall optimization process can be summarized as follows:

1. The optimization process starts by performing an initial sampling of the propeller design space using the Latin Hypercube Sampling (LHS) method. Typically, the initial design set contains several hundred different propeller blade designs.

2. Each individual design from the initial design set is exported using `.stl` CAD files and meshed in ANSYS ICEM CFD.

3. ANSYS CFX simulates the flow field around each design in the initial design set. After convergence has been reached the solver outputs the values of thrust coefficient C_T and propeller efficiency η.

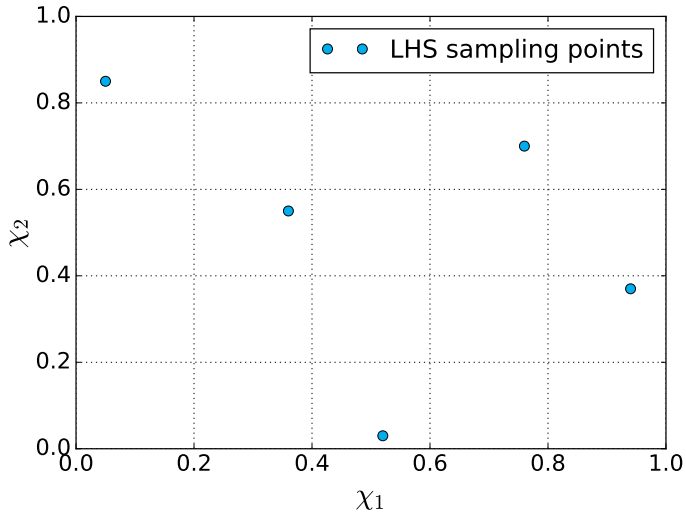

Figure 4.2.1: *Five point LHS sampling of the space spanned by variables χ_1 and χ_2.*

4. A meta-model is constructed using the design variables, thrust coefficient, and propeller efficiency of the entire initial design set. The meta-model will later be used by the GA as a fast means to evaluate the performance of new designs without using CFD.

5. The task of the GA is now to find new designs with maximized C_T and η. This step in the optimization process is iterative, and involves tens of thousands of objective function evaluations, which prohibits the direct use of CFD. Instead, the meta-model is used to estimate the values of C_T and η for each new individual design. The main output of this step in the optimization is a group of new, prospectively optimal candidate designs. These are then in turn meshed, simulated using CFD, and their performance values added to the meta-model.

The optimization loop iterates until the meta-model converges or until no improvement in the objective functions is observed for a pre-defined number of iterations. The optimizations performed as part of this thesis all optimize propeller efficiency and thrust coefficient, which results in large databases of optimal designs with varying levels of thrust. The information in these databases can then be used for sizing propellers for different applications, such as for a given engine thrust on a single rotating propeller, or for choosing the appropriate front rotor in a CROR.

4.2 Latin Hypercube Sampling

The first step of the optimization platform is to create an initial design set by means of a Latin Hypercube Sampling (LHS) technique, exemplified in Fig. 4.2.1. This technique

randomly samples the K-dimensional design space with a pre-determined number of samples $\mathcal{N}_{samples}$ (initial designs). The LHS divides the ranges of the design variables χ_i into $\mathcal{N}_{samples}$ equidistant subranges, and only allows one sample point to occupy each subrange. Additionally, the placement of the sample point inside the subrange itself is randomized. In this way, each design variable is well-sampled and the design space in randomly searched. The number of required samples is calculated using Eq. 4.2.1 by assuming that the topology of the response surface $f(\chi_1, \chi_2, ..., \chi_K)$ of the objective function is similar to the K-dimensional quadratic polynomial given in Eq. 4.2.2.

$$\mathcal{N}_{samples} = \frac{(K+1)(K+2)}{2} \tag{4.2.1}$$

$$f(\chi_1, \chi_2, ..., \chi_K) = \sum_{i,j=1}^{K} (A_{ij}\chi_i\chi_j + B_i\chi_i) + C \tag{4.2.2}$$

4.3 Meta-model

All designs that are simulated using CFD within the optimization framework are added to a database which is used to build a meta-model. Given a set of propeller design parameters, the meta-model can very quickly and efficiently estimate values of the objective functions compared to using CFD directly. This ability is exploited by the GA in order to identify new prospective designs which should be simulated with CFD.

The meta-model used in this thesis is of the Radial Basis Function (RBF) type, building upon the in-house experience and research on the optimization of transonic compressors [36, 37, 48–51]. The RBF is a type of interpolation method where the response surface value $f(\mathbf{x})$ for a point $\mathbf{x}$ is a function of its Euclidean distance r_j from the $\mathcal{N}_{DP}$ known data points. For each known data point $\mathbf{x}_j$, there is an associated weight w_j, and basis $b(r_j)$, which is used to calculate the response surface value $f(\mathbf{x})$:

$$f(\mathbf{x}) = \sum_{j=1}^{\mathcal{N}_{DP}} w_j b(r_j) \tag{4.3.1}$$

$$r_j = ||\mathbf{x} - \mathbf{x}_j|| \qquad \mathbf{x} = [\chi_1, \chi_2, ..., \chi_K] \tag{4.3.2}$$

For the purpose of this work, K corresponds to the number of design variables in the optimization. Various types of bases $b(r_j)$ can be used in the RBF, of which the multiquadratic (Eq. 4.3.3), inverse (Eq. 4.3.4), and Gaussian (Eq. 4.3.5) are used here:

$$b(r_j) = \sqrt{(r_j/\varepsilon)^2 + 1} \tag{4.3.3}$$

$$b(r_j) = 1/\sqrt{(r_j/\varepsilon)^2 + 1} \tag{4.3.4}$$

$$b(r_j) = e^{-(r_j/\varepsilon)^2} \tag{4.3.5}$$

The value of the bases $b(r_j)$ and tuning parameter ε can result in different response surfaces, as is shown in Fig. 4.3.1. Therefore an algorithm for finding the best combination of basis and tuning parameter is used:

1. Use most of the data points for establishing the RBF, but exclude a fraction of them for later. This fraction is typically $10 - 20\%$.

2. Construct the RBF using the three bases in Eq. 4.3.3 to 4.3.5 and different values of the tuning parameter ε.

3. The excluded data points from step 1 are now compared to their estimated values using the constructed RBFs.

4. Choose the combination of basis and ε which produces the lowest RMS-error.

Now that the tuning parameter ε and basis have been determined, the value of the weights w_j can be obtained by applying Eq. 4.3.1 on the known data points, thereby producing a linear system of equations:

$$f_i(\mathbf{x}_i) = \sum_{j=1}^{\mathcal{N}_{DP}} w_j \phi(r_{ij}) \qquad i, j = 1, 2, ..., \mathcal{N}_{DP} \tag{4.3.6}$$

$$r_{ij} = ||\mathbf{x}_i - \mathbf{x}_j|| \tag{4.3.7}$$

This system is easily solved for the weights w_j since both the data points x_i and the response surface value f_i are known. After the RBF is established, the GA uses it for evaluating the objective functions of any design without requiring time-consuming CFD simulations.

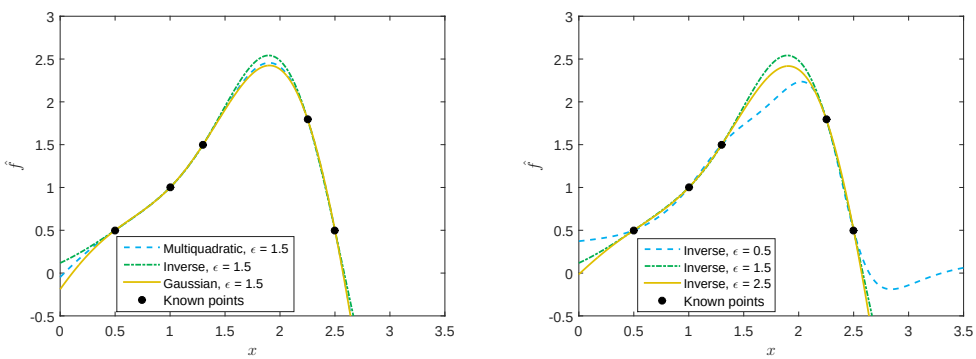

(a) **(b)**

Figure 4.3.1: *The effect on the response surface f for choosing different* ***(a)*** *basis and* ***(b)*** *tuning parameter ε for a one-dimensional RBF.*

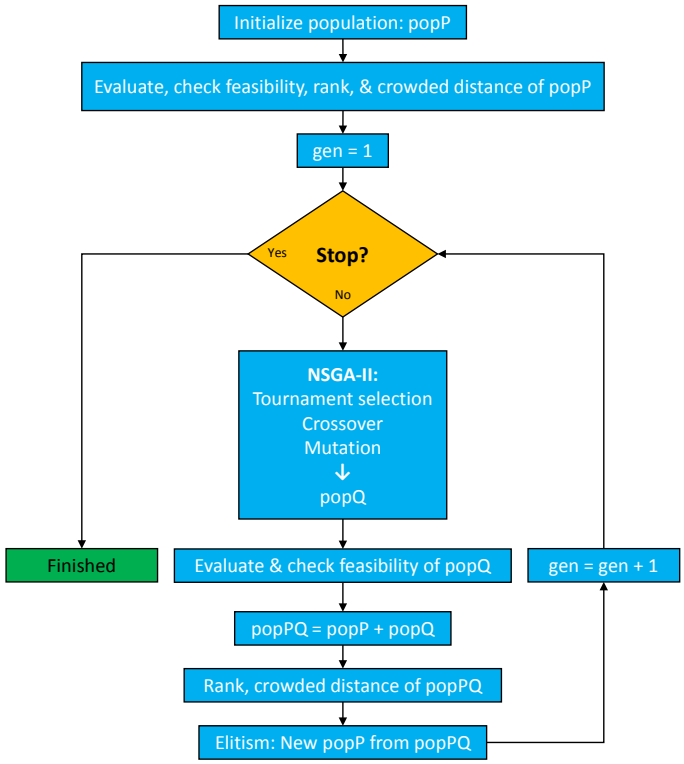

Figure 4.4.1: *The structure of the GA.*

4.4 Genetic Algorithm

After constructing the meta-model (see Fig. 4.1.1) an optimizer is needed for finding new, optimal designs. Classical optimization is often deterministic and gradient-based, which can result in clustering of designs in local optima rather than the sought-after global optimum. In contrast, stochastic optimization methods such as Genetic Algorithms (GA), particle swarm optimization, and ant colony optimization all contain stochastic operators which allows the optimizer to explore other parts of the design space, therefore avoiding getting trapped in local optima.

In this thesis, a GA based on the multi-objective NSGA-II optimization algorithm [47] has been chosen for the aerodynamic optimization of high speed propellers. This type of algorithm has previously been shown to be effective for cases involving the aerodynamic optimization of transonic compressors [36, 37, 48–51] and contains processes such as selection, crossover (reproduction), and mutation which mimic the biological concepts which are integral parts of the evolutionary process in nature.

The various processes which are incorporated into the GA algorithm are shown in Fig. 4.4.1. The first step of the algorithm is to create an initial population *popP* consisting of $\mathcal{N}_{GA}$ individual propeller designs, whose design data is encoded in strings of digits

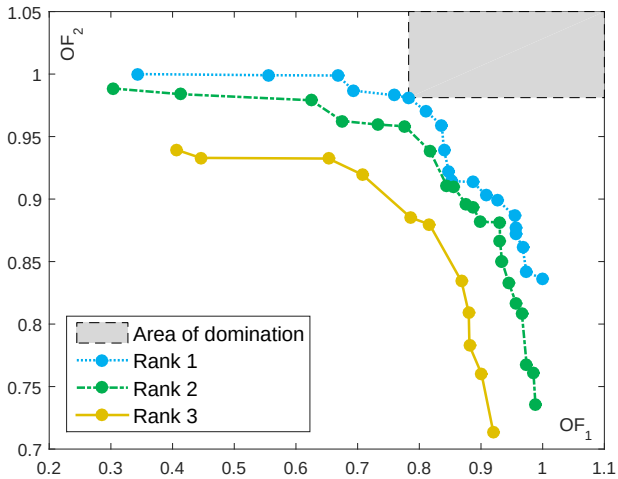

Figure 4.4.2: *Population ranking for a multi-objective optimization for the case of maximizing objective function 1 (OF_1) and objective function 2 (OF_2). The gray area is the area of domination for a specific individual, and if no other individual is inside this area the specific individual is said to be non-dominated, and therefore optimal.*

which are referred to as chromosomes. These chromosomes are used to represent the numerical values of the design variables since they allow for easy definition of crossover and mutation processes later on. The fitness of each member in the initial population *popP* is then evaluated using the meta-model, its feasibility checked, and its ranking established. A central concept in this part of the optimization algorithm is ranking, which determines how optimal a design is. For the multi-objective optimizations performed in this thesis ranking is performed using the approach of non-domination, which for a two-objective function optimization is illustrated in Fig. 4.4.2. In this case the aim of the optimization is to maximize the objective functions OF_1 and OF_2 and Rank 1 is the group of designs in the population which are optimal, and define the Pareto front of the population. For any design in Rank 1 an area of non-domination (gray box) can be constructed. Since no other design resides in this area, it is said to be non-dominated, and therefore optimal. If Rank 1 designs are subtracted from the population, then a new group can be selected which is non-dominated. This group is then Rank 2, and is only dominated by Rank 1. By subtracting Rank 1 and 2 from the population a Rank 3 can be constructed, and so on and so forth until the entire population has been ranked. In order to sort individuals inside each rank from best to worst, a crowded distance measure is used within each rank. This measure estimates how crowded the region is around each individual, and sorts all designs from best to worst based on how large the distance is to its neighbors. The crowded distance parameter ensures a good spread of solutions along each rank.

Now that the population *popP* has been ranked from best to worst a new population,

popQ, will be created by applying selection, crossover, and mutation. Tournament selection with a size of two is used in this thesis, and a one-point crossover process is used to represent biological reproduction. When the creation of popQ is finished, its individuals are evaluated using the meta-model and it is joined with the individuals in *popP* to form population *popPQ*. By joining these two populations, the best designs of each generation (Rank 1 of *popP*) is saved, which is commonly referred to as *elitism*. The aggregate population *popPQ* is then ranked, and $\mathcal{N}_{GA}$ individuals are taken from it, starting with the best until the new population *popP* is full.

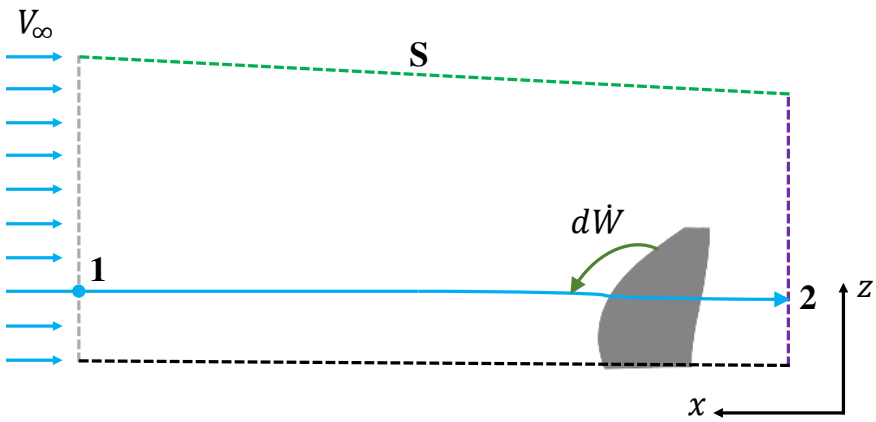

Figure 5.1.1: *Control volume for wake analysis. Surface 1 (gray) is assumed to have uniform properties while the streamsurface S (green) has no mass flux crossing it. A streamline travelling from 1 to 2 (purple) has been added to illustrate the work transfer from a propeller blade to the flow.*

5 Wake Analysis Method

The *Wake Analysis Method* (WAM) was developed in order to quantify the energy content of the wake structures found in Boxprops and conventional propellers in terms of propeller shaft power, allowing different types of propellers to be analyzed and their losses compared on equal terms. The method provides a systematic breakdown of the work added by the propeller (shaft power) to the flow into entropy lost work, reversible pressure changes, and kinetic and turbulent energy changes. The magnitude of these terms provide insight into how much of the work added by the propeller is propulsively beneficial, recoverable in a downstream rotor, or pure losses. A velocity decomposition is also introduced which clearly distinguishes the tip vortices and wakes from the mean flow, which is then used for estimating the strength of these flow features in terms of shaft power.

5.1 Derivation

For a control volume enclosing the propeller blade (see 5.1.1) there are three surfaces. Surface 1 is located far upstream of the propeller and has uniform properties equal to their freestream values. Surface S is defined as a streamsurface with no mass flux across it, and Surface 2 is located downstream of the propeller and its flow properties are not uniform. With the two conditions imposed on Surface 1 and Surface S, a control volume analysis yields that the shaft power P_{shaft} input into the control volume equals the mass

flow integral of the total enthalpy change on surface 2:

$$P_{shaft} = \int_2 \Delta h_0 d\dot{m} = \int_2 (h_{02} - h_{01}) d\dot{m} \tag{5.1.1}$$

Here the change in total enthalpy denotes the change between positions on plane 2 and the constant freestream properties, which is denoted as h_{01}. Constructing a control volume with surface 1 far upstream with uniform flow properties and surface S as a streamsurface reduces the entire control volume analysis to only a surface integral evaluated on surface 2. The change in total enthalpy in the control volume is accounted for by calculating the change in total enthalpy $\Delta h_0 = h_{02} - h_{01}$, where index 1 denotes the freestream values. An identical expression to Eq. 5.1.1 is obtained if one follows a streamline for an elemental fluid particle travelling from a surface far upstream (1) to a surface downstream of the rotor (2), as is illustrated in Fig. 5.1.1 and shown in Eq. 5.1.2.

$$d\dot{W} = (h_{02} - h_{01}) d\dot{m} \tag{5.1.2}$$

Hence:

$$P_{shaft} = \int_2 d\dot{W} = \int_2 \Delta h_0 d\dot{m} = \int_2 (h_{02} - h_{01}) d\dot{m} \tag{5.1.3}$$

The change in total enthalpy can be expanded into its constituents as is shown in Eq. 5.1.6, and can be expanded further into an irreversible entropy lost work term ϕ_s and a reversible pressure work term ϕ_p using the Gibbs relation in Eq. 5.1.5.

$$dh = Tds + \nu dp \tag{5.1.4}$$

$$\rightarrow \Delta h = h_2 - h_1 = \underbrace{\int_1^2 Tds}_{\phi_s} + \underbrace{\int_1^2 \nu dp}_{\phi_p} \tag{5.1.5}$$

$$\Delta h_0 = \underbrace{(\phi_s + \phi_p)}_{\Delta h} + \Delta(\frac{1}{2} u_i u_i) + \Delta k \tag{5.1.6}$$

The entropy lost work term ϕ_s is evaluated using the approach used by Hall [22], Denton [52], Dixon [53], and Miller [54], while the pressure work term ϕ_p is obtained by subtracting the entropy lost work term from the static enthalpy change:

$$\phi_s = \int_1^2 Tds \approx T_\infty (s_2 - s_1) \tag{5.1.7}$$

$$\phi_p = \int_1^2 \nu dp \approx (h_2 - h_1) - T_\infty (s_2 - s_1) \tag{5.1.8}$$

The kinetic energy term in Eq. 5.1.6 can be expanded to include the axial, radial, and swirl velocities:

$$\frac{1}{2}u_i u_i = \frac{1}{2}\left(u_x^2 + u_r^2 + u_\theta^2\right) \tag{5.1.9}$$

The changes in kinetic energy can be written as the differences between the downstream values (2) and the upstream values (1), assuming that no radial and swirl velocities exist in the freestream:

$$\Delta\left(\frac{1}{2}u_i u_i\right) = u_{x,1}\Delta u_x + \frac{1}{2}\left((\Delta u_x)^2 + u_{r,2}^2 + u_{\theta,2}^2\right) \tag{5.1.10}$$

$$\Delta u_x = u_{x,2} - u_{x,1}$$

Including all the expressions for entropy lost work, pressure work, and kinetic energies results in the following equation:

$$P_{shaft} = \int_2 \left[\phi_s + \phi_p + u_{x,1}\Delta u_x + \frac{1}{2}\left((\Delta u_x)^2 + u_{r,2}^2 + u_{\theta,2}^2\right) + (k_2 - k_1)\right] d\dot{m} \tag{5.1.11}$$

In order to capture the structure of the wake and tip vortex, the velocities $u_i\,(r,\theta)$ are decomposed into a *circumferentially averaged velocity* $U_i\,(r)$ and an associated *perturbation* $v_i\,(r,\theta)$:

$$u_i\,(r,\theta) = U_i\,(r) + v_i\,(r,\theta) \tag{5.1.12}$$

$$U_i = \tfrac{1}{\kappa}\int_0^{2\pi} \rho_2 u_n u_i d\theta \quad \kappa = \int_0^{2\pi} \rho_2 u_n d\theta \tag{5.1.13}$$

Including this velocity decomposition into Eq. 5.1.11 yields:

$$P_{shaft} = \int_2 \Big[\phi_s + \phi_p + u_{x,1}\Delta u_x + \frac{1}{2}\left((\Delta U_x)^2 + U_{r,2}^2 + U_{\theta,2}^2\right) + \frac{1}{2}\left((\Delta v_x)^2 + v_{r,2}^2 + v_{\theta,2}^2\right) + (k_2 - k_1)\Big] d\dot{m} \tag{5.1.14}$$

Green terms of Eq. 5.1.14 constitute the propulsive power, red terms constitute losses, and blue terms represent recoverable kinetic energy. An explanation of the physical nature of each term is provided below:

- The entropy lost work term ϕ_s is a thermodynamic loss and increases when the flow experiences shocks, mixing, and viscous losses in boundary layers and shear layers.
- Thrust is represented by the pressure work term ϕ_p and axial momentum change $u_{x,1}\Delta u_x$. For a fully expanded jet slipstream the axial momentum change fully accounts for the produced thrust and propulsive power, but in proximity to the blade the pressure is not yet the same as in the freestream, and therefore the pressure work

terms needs to be included. The pressure term ϕ_p increases when the flow passes through the propeller disk and decreases downstream, while the axial momentum experiences a corresponding increase. This is in accordance with simpler propeller theories such as the Actuator Disk Theory.

- The term $(\Delta U_x)^2/2$ represents the excess axial kinetic energy found in the jet downstream of the rotor. The mean radial $(\Delta U_r)^2/2$ kinetic energy is also a loss while the swirl $(\Delta U_\theta)^2/2$ kinetic energy could be recovered in a downstream stator or counter-rotating propeller.

- The kinetic energy bounded to the perturbations of the flow $((\Delta v_x)^2 + v_{r,2}^2 + v_{\theta,2}^2)/2$ – in this case propeller wakes and tip vortices – is a pure loss.

- The change in turbulent kinetic energy $(k_2 - k_1)$ occurs mostly in the boundary and shear layers in the flow. Eventually this term dissipates and is converted into entropy lost work. This term was shown to be quite small ($< 0.5\%$ of shaft power) in Paper II and is usually omitted from the rest of the analysis.

5.2 Effect of the integration surface size

It is important to note the effect of the integration surface size on the terms of the wake analysis. A small radius (see the red lines in Fig. 3.3.2) for the integration surface could possibly miss important flow features, while a large radius makes the surface come close to the frozen rotor interfaces. In order to investigate the effect of this, Paper VII included a small comparison of the wake analysis terms in Eq. 5.1.11 (excluding the turbulent kinetic energy) for four different integration surface radii. The comparison was done for the optimized Boxprop with ID-name *BP1112* which is analyzed in detail in Paper VII.

The differences in the wake analysis terms for each surface for the *BP1112* Boxprop are shown in Table 5.2.1, where the difference versus the largest surface has been used. As can be seen, the difference in total enthalpy change is very small between the analyzed planes, with a change of -0.09% of engine shaft power between the smallest and largest plane. For ϕ_p the value changes with -8.70% of shaft power for the smallest relative to the largest surface, while for the axial momentum term $u_{x,1}\Delta u_x$ this behavior can be seen to act in the opposite direction, so that the axial kinetic term changes with $+9.19\%$ of engine shaft power from the smallest to the largest plane. This is expected since the pressure field from the propeller extends quite far out from the propeller. The size of the integration surface seems to affect the relative amount of shaft power input into either ϕ_p or $u_{x,1}\Delta u_x$, but their sum which constitutes the propulsive power stays relatively constant with respect to integration surface size. The loss terms which are the ones most often compared between differente designs, namely entropy lost work ϕ_s , excess axial kinetic energy $(\Delta u_x^2)/2$, radial kinetic energy $u_r^2/2$, and swirl kinetic $u_\theta^2/2$ energy differ by less than 0.25%. In conclusion, it is critical to use identical integration surface sizes in order make a fair comparison between two different propeller types, a conclusion which was also reached in Paper IV of this thesis for a similar wake analysis for naval propellers. For the work included in this thesis regarding aero engine propellers an integration surface

size of $1.8R$ is used, as has been shown in Fig. 3.3.2, which places the outer radius of the integration surface one blade height away from the frozen rotor interface.

Table 5.2.1: Integration surface size effect on the wake analysis terms. The values are written as percentages of shaft power P_{shaft}, and calculated as the finite difference relative to the largest surface (Surf 4). The surfaces of integration are located $0.05D$ from the trailing edge of the *BP1112* Boxprop from Paper VII at the 75% radial position.

$\frac{1}{P_{shaft}}\int_2 \varphi d\dot{m}$		Surf 1 $1.2R$	Surf 2 $1.5R$	Surf 3 $1.8R$	Surf 4 $2.1R$
$\varphi =$	Δh_0	-0.09%	-0.03%	-0.03%	-
	ϕ_s	-0.10%	-0.10%	-0.07%	-
	ϕ_p	-8.70%	-4.18%	-1.54%	-
	$u_{x,1}\Delta u_x$	$+9.19\%$	$+4.56\%$	$+1.71\%$	-
	$\phi_p + u_{x,1}\Delta u_x$	$+0.49\%$	$+0.38\%$	$+0.18\%$	-
	$(\Delta u_x^2)/2$	-0.16%	-0.11%	-0.04%	-
	$u_r^2/2$	-0.25%	-0.16%	-0.08%	-
	$u_\theta^2/2$	-0.07%	-0.04%	-0.01%	-

6 Summary of Papers

6.1 Paper I

R. Avellán, A. Capitao Patrao, A. Lundbladh, and T. Grönstedt, 2015, Preparing for Proof-of-Concept of a Novel Propeller for Open Rotor Engines, *22nd ISABE Conference*, October 25–30, Phoenix, USA.

6.1.1 Summary

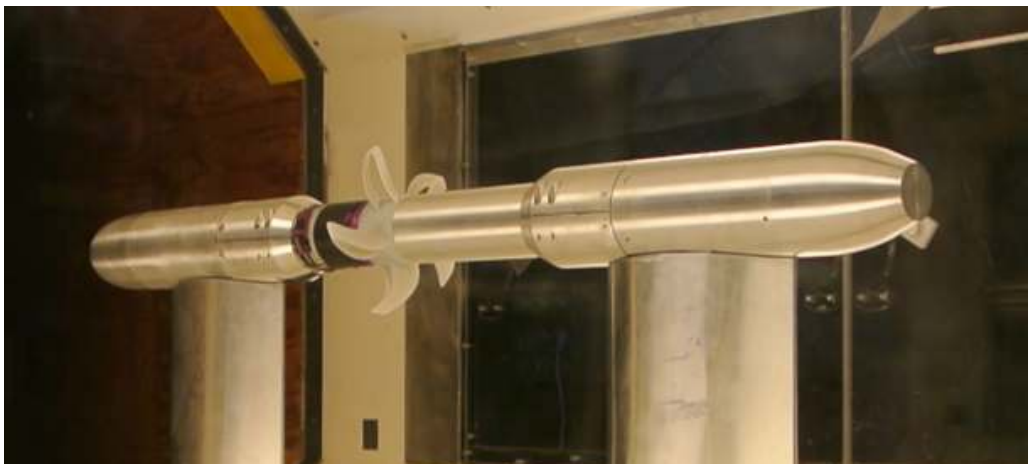

Figure 6.1.1: *The 150 mm diameter GP-X-313 Boxprop mounted on the propeller testing rig. Flow goes from left to right.*

This paper summarizes the development of the Boxprop during the period between 2013 and 2015 with a focus on manufacturing techniques for small scale test propellers and their aerodynamic performance. Data from experimental testing (see Fig. 6.1.1) at take-off conditions of 3D-printed propellers is compared to numerical simulations for the sake of validation of the numerical approach. An early version of the Wake Analysis Method is also presented.

New insights gained from a student project on the manufacturing of metallic small scale propellers is presented. The choice of manufacturing process (multi-axis milling, Electron Beam Melting (EBM), and Selective Laser Melting (SLM)) and its effect on cost, surface finish, and lead times is presented. The milled blades had excellent surface finish, but longer lead times and five times higher cost than an entire 3D-printed plastic propeller. The blades manufactured with additive methods (EBM and SLM) had lower lead times and were cheaper than the milled blade, but unfortunately possessed a much higher surface roughness, thus requiring polishing after-treatments.

The development of Boxprop design for cruise is presented in terms of efficiency and

thrust. These two performance parameters have increased substantially since the start of the research project, and the underlying flow features and geometric changes that have led to these increases in performance are presented. The two main design changes is the tailoring of the tip of the Boxprop to the oncoming flow, and the use of different camber and angle-of-attack distributions for the two blade halves, which decreases some of the interference in the blade passage.

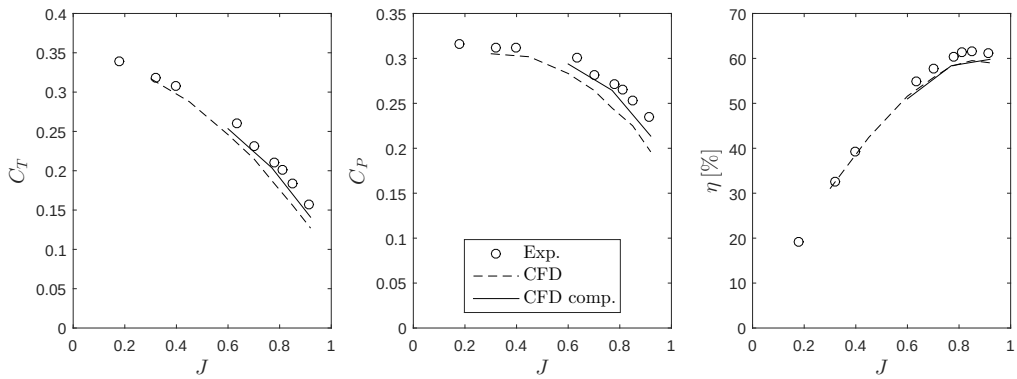

Figure 6.1.2: *Propeller thrust coefficient, power coefficient, and propeller efficiency as function of the advance ratio J.*

Propeller performance for the GP-X-313 Boxprop at low axial speed conditions is summarized in Fig. 6.1.2 for both experiments and simulations. Note that the values in this figure are slightly different compared to the figures in Fig. 11 and 12 in Paper I. This is due to the fact that the values included here in Fig. 6.1.2 have been compensated for motor induced torque in the rig, pressure differences in upstream and axial hub surfaces, and adjusted using the Glauert [55] wind speed compensation formula:

$$V_\infty = V_{up}\left(1 - \frac{\mathcal{K}_T}{2\sqrt{1+\mathcal{K}_T}}\right)\left(\frac{A_p}{A_{WT}}\right) \qquad \mathcal{K}_T = F_x/\rho A_p V_{up}^2 \tag{6.1.1}$$

This formula corrects the velocity used in the calculation of the advance ratio $J = V_\infty/nD$ using the measured velocity in the tunnel V_{up}. Overall, the obtained experimental and numerical results in Fig. 6.1.2 show good agreement. The trends match and the absolute values are similar. The performance values are shown for varying advance ratio J, which was adjusted by changing the freestream axial velocity and keeping the rotational velocity constant. There are two CFD cases, the first being a simulation using a propeller with a hydraulically smooth surface, a simple cylindrical hub, and no deformation due to centrifugal stresses. The second case (*compensated CFD*), includes surface roughness, the real nacelle geometry used in experiments and blade deformation. The similarity of the computational and experimental data for the GP-X-313 increases the confidence of the adopted CFD methodology. Unfortunately, the Chalmers Wind Tunnel cannot achieve high enough axial Mach numbers for validation of the CFD simulations at cruise conditions. Nevertheless, this work shows very good agreement between experiments and

CFD at near take-off conditions.

An early version of the Wake Analysis Method was presented and derived in this paper. The velocity was shown be decomposable into a circumferential average and an associated perturbation, of which the latter clearly accounts for velocities in tip vortices and wakes behind a propeller, as is shown in Fig. 6.1.3. Very brief results from this theory were presented for a generic conventional propeller based on the NASA SR7L propeller.

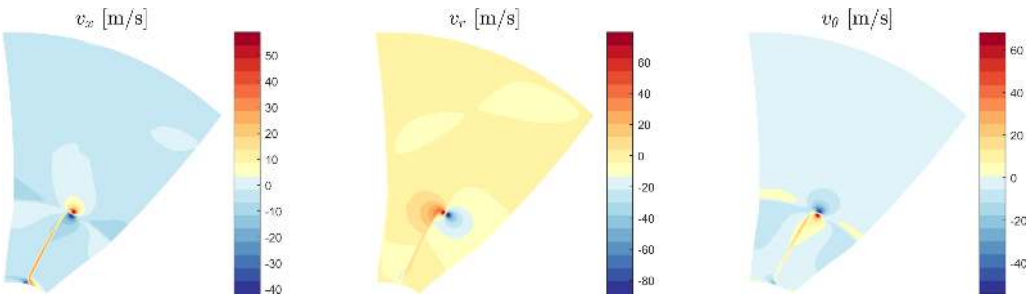

Figure 6.1.3: *The velocity perturbations on planes normal to the axial direction at a downstream distance of* $0.15D$ *from the propeller blade.*

6.1.2 Division of work

In this paper I supervised the experimental and computational work which compared the performance obtained with CFD and the Chalmers Wind Tunnel. I also perfomed the design, meshing, and simulation of the GP-X-701 propeller at cruise conditions and developed initial versions of the Wake Analysis Method together with Anders Lundbladh. My co-authors contributed with insights and analysis of the obtained numerical and experimental results. Richard Avellán was the main author of the paper, and coordinated the work on material selection, manufacturing processes, and pitch mechanisms for small scale propellers, which was performed by a group of students from the Chalmers Product Development Master's programme.

6.2 Paper II

A. Capitao Patrao, R. Avellán, A. Lundbladh, and T. Grönstedt, 2016, Wake and Loss Analysis for a Double Bladed Swept Propeller, *Proceedings of ASME Turbo Expo 2016*, June 13–17, Seoul, South Korea.

6.2.1 Summary

The main aim of this paper was to highlight the differences in the wake between a conventional propeller and the Boxprop, and use this information as guidance for future, improved designs. The geometries of the conventional propeller GP-S-609 and the Boxprop GP-X-701 are described in relatively high detail, as is the adopted computational method. Results from the Wake Analysis Method are presented here in order to better understand the magnitude of the different sources of loss for the propellers.

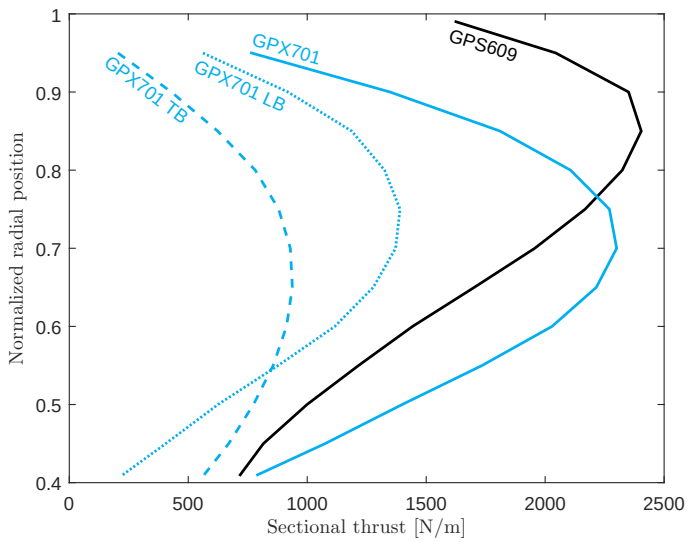

Figure 6.2.1: *Sectional thrust F'_x for the GP-S-609 and the GP-X-701 propellers. The Boxprop sectional thrust is also decomposed into thrust produced at the LB and TB.*

Performance-wise, the GP-X-701 Boxprop can provide the necessary thrust to replace the front rotor of modern, published CROR designs. The major caveat is the higher amount of swirl compared to the GP-S-609 propeller, which is evident both in the location of the peak sectional thrust in Fig. 6.2.1 and in the Wake Analysis results in Fig. 6.2.3. This higher amount of swirl could partially be recovered in the rear, counter-rotating propeller of a CROR. The major reason that this particular Boxprop design is more highly loaded closer to the hub is the blade interference in the blade passage. The interference is most pronounced in the upper half of the blade, and is manifested by the high Mach number and low pressure region in the blade passage seen in Fig. 6.2.2. At

a non-dimensional radius of $\xi = 0.75$ a region of high Mach number is seen to extend from the suction side of the leading blade to the pressure side of the trailing blade. This reduces the amount of obtainable lift (and thrust) for the TB, thereby lowering efficiency. This blade interference therefore prevents the trailing blade from producing any large amount of thrust if it lies in close proximity to the leading blade.

In this paper and in Fig. 6.2.3 the WAM shows clearly the main energy transfer process occurring downstream of the propeller, specifically between static pressure and axial kinetic energy, which is in accordance to existing propeller models such as the Actuator Disc Model. In this paper, pressure energy could not yet be separated from static enthalpy as was described in Chapter 5, so the decrease in static enthalpy in Fig. 6.2.3 contains both the decrease in pressure energy and increase in entropy lost work. Nevertheless, the method was used to quantify the fraction of engine power that was transferred to the kinetic energy of swirl (which is recoverable) and to the wakes and tip vortices (which is not recoverable). The kinetic energy of the perturbations as a fraction of engine power is shown to be similar in magnitude for both propellers, but is slightly lower for the Boxprop where a possible rear rotor would be located.

The last major conclusion of this paper was the lack of tip vortex for the analyzed GP-X-701 Boxprop at the cruise operating condition. When comparing perturbation velocities, streamline plots, and vorticity plots it is evident that that this Boxprop does not produce a traditional, near-circular tip vortex, instead the tangential perturbation velocity is more spread around the arc-shaped tip of the Boxprop. This might give some insight into how the Boxprop could perform from an acoustic point-of-view. Lower and more spread out perturbation velocities might result in lower amounts of noise when these flow perturbations impinge on a rear, counter-rotating propeller.

6.2.2 Division of work

Besides being first author, my contribution was designing both the conventional propeller and the Boxprop, performing their meshing, and simulation. Additionally, I developed procedures and scripts for sampling data in the CFD results for the WAM. A significant amount of time and effort went into finding the right mesh for this method, particularly in terms of mesh convergence. My co-authors supervised my work and aided in the analysis of the results. My co-authors also contributed with large parts of the introduction, discussion, and conclusions.

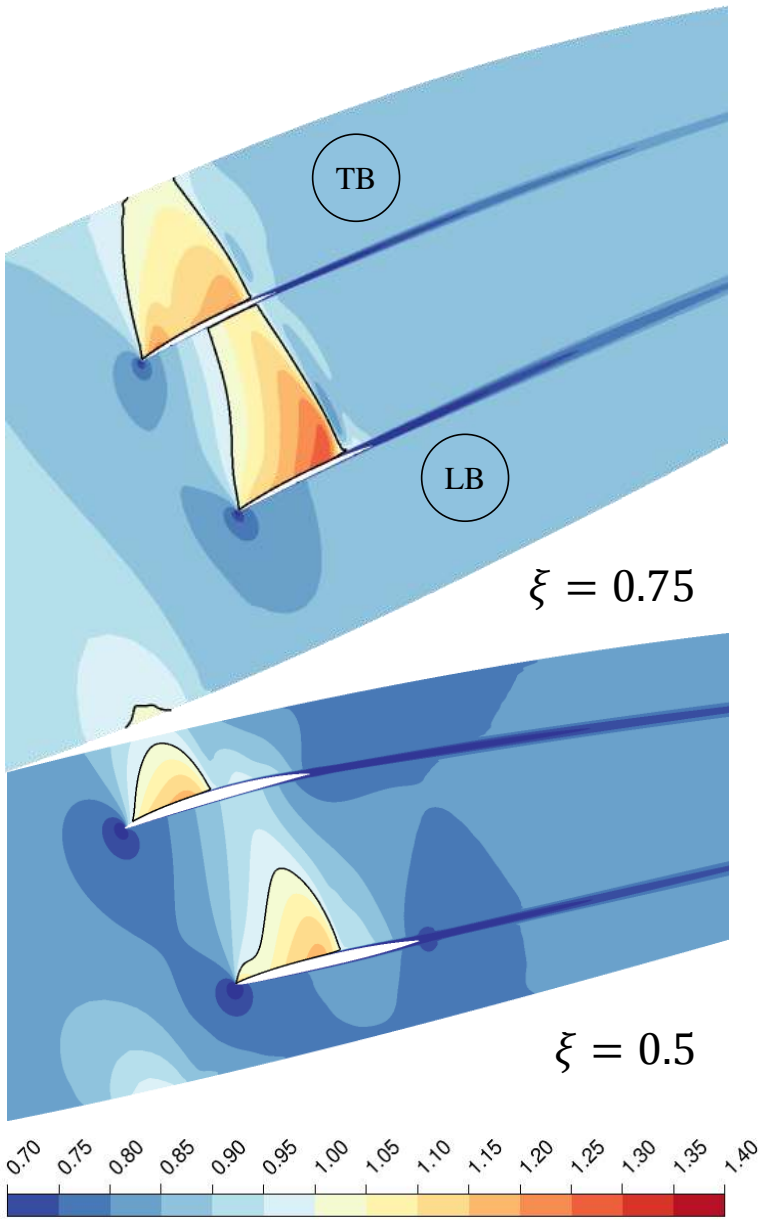

Figure 6.2.2: *Mach number contour for the GP-X-701 at non-dimensional radius* $\xi = r/R = 0.5$ *and* $\xi = r/R = 0.75$*. Solid lines denotes Mach 1, which also denotes the location of shocks whenever the upstream flow is supersonic.*

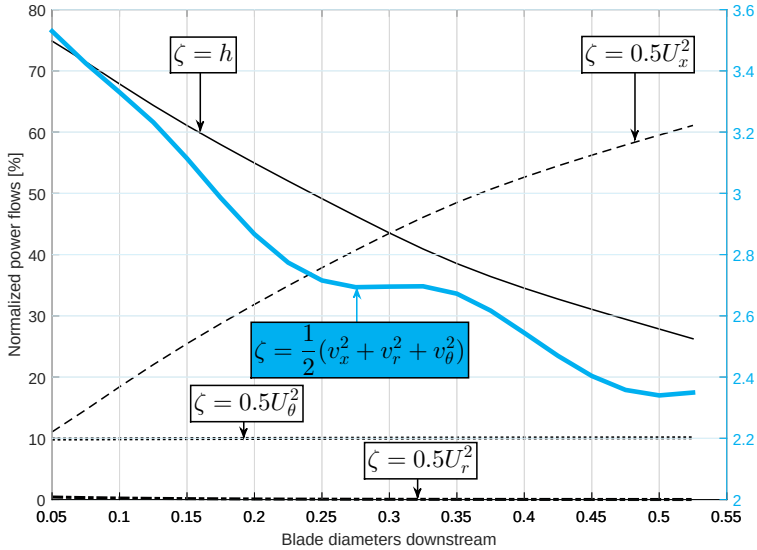

(a) *GP-S-609*

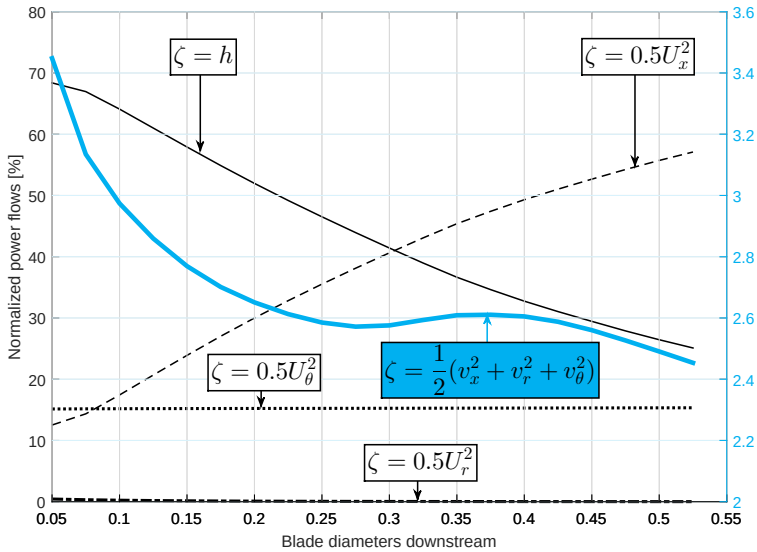

(b) *GP-X-701*

Figure 6.2.3: *Power integrals $\int \Delta\zeta d\dot{m}$ normalized by shaft power as a function of axial distance for the* ***(a)*** *GP-S-609 and* ***(b)*** *GP-X-701 propellers. The kinetic energy bounded to the perturbation velocities are plotted in blue on separate axes.*

6.3 Paper III

A. Capitao Patrao, G. Montero Villar, J. Takachi Tomita, C. Bringhenti, R. Avellan, A. Lundbladh, and T. Grönstedt. "An Optimization Platform for High Speed Propellers", *Aerospace Technology Congress*, 11-12 October 2016, Solna, Stockholm.

6.3.1 Summary

In this paper an optimization platform is presented for the aerodynamic optimization of the Boxprop. Results for an optimization effort with a limited amount of design variables and with the aim of maximizing thrust and efficiency showed modest improvements in efficiency and lower amounts of downstream swirl when compared to older Boxprop designs, thereby demonstrating the effectiveness of the optimizer.

The complex and highly three-dimensional shape of the Boxprop renders classic propeller design methods such as the Blade Element Momentum (BEM) [33], vortex [34], and lifting line [21] ineffective. Paper I showed that different distributions of angle-of-attack and camber are needed for each blade half due to blade interference, which cannot be accounted for using the classical BEM/Vortex methods. The cruise operating point for the Boxprop entails transonic flow over large regions of the blade and occasionally choked sections of the blade passage, which invalidates the use of lifting line methods, which have otherwise been used successfully for the design of conventional open rotor blades [21]. With this in mind, a Boxprop optimization platform was developed, whose principal components have been described in Chapter 4. The optimization platform is coded in Python and contains the functionality for geometry generation, mesh generation (using ICEM CFD), CFD pre-processing, job management in conjunction with the Chalmers C3SE computing cluster, post-processing, and optimization.

Critical to the success of the optimization was the developed design parametrization, which has two distinct parts, the first being the parametrization of the Boxprop stacking line, and the second being the parametrization of the distributions of profile chord, camber, and angle-of-attack. These are described in detail in Chapter 2.

A major improvement in the work flow was achieved by automating the geometry and mesh generation, enabling the simulation of the hundreds of CFD cases needed for the optimization platform. This was achieved by using the Python module numpy-stl for exporting the blade geometries in the `.stl` CAD format. Meshing scripts are also generated for the automated blocking and meshing of the Boxprop using ICEM CFD, resulting in a reduction in CFD pre-processing from several days to 5-10 minutes per case.

The optimization platform was unleashed on the Boxprop with the objectives of maximizing propeller efficiency and thrust at cruise. In total, 17 optimization variables were used for demonstrating the optimization platform, while the chord, camber, and thickness distributions were kept fixed. As shown in Fig. 6.3.1, a modest improvement in propeller efficiency of 1.3% was achieved relative to the GP-X-701 Boxprop for the thrust coefficient $C_T = 0.484$. The optimized Boxprop geometries show higher efficiency, less swirl, and less blade interference than previous designs due to the new stacking line parametrization. The optimization platform has clearly demonstrated its effectiveness in this paper, and is the foundation for the subsequent research regarding the Boxprop.

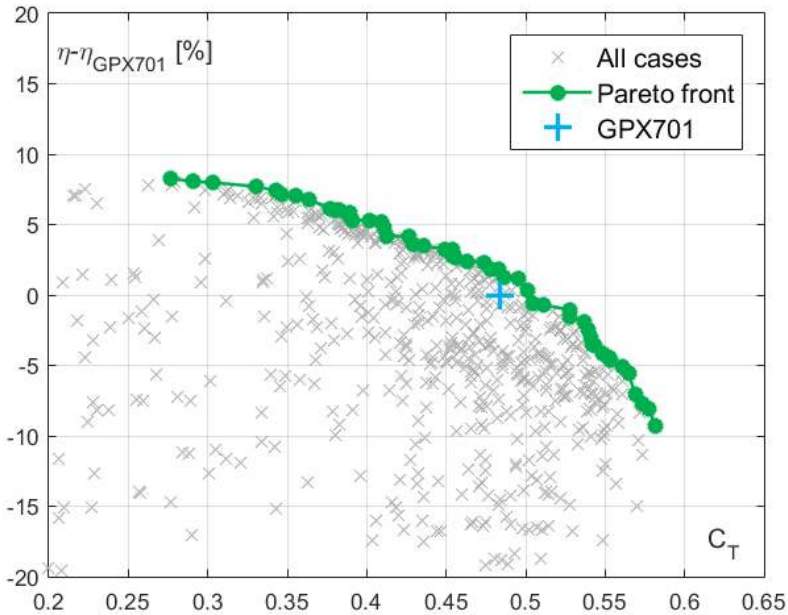

Figure 6.3.1: *All 740 propeller designs that have been evaluated using CFD, the obtained Pareto front, and the GP-X-701 performance. All efficiency values have been normalized with the GP-X-701 propeller efficiency in order to illustrate the improvement.*

6.3.2 Division of work

The Boxprop optimization platform described in this paper was co-developed by myself and Gonzalo Montero Villar, whom I supervised together with Marcus Lejon during his Master's Thesis project in 2016. The simulations were performed jointly by me and Gonzalo, while the paper was written by me with feedback and support from Gonzalo and the other co-authors. My co-authors also provided insight into the results and in drawing conclusions.

6.4 Paper IV

Andersson, J., Eslamdoost, A., Patrao, A. C., Hyensjö, M., and Bensow, R. E. "Energy Balance Analysis of a Propeller in Open Water", *Ocean Engineering*, 158, 162-170, 2018.

6.4.1 Summary

An energy balance method is presented in this paper which is able to account for all the hydrodynamic losses present in a propeller in open water. The method is derived and applied on a simplified case consisting of a propeller and a streamlined cylindrical hub.

The energy balance method is derived from the Reynolds Transport Theorem for energy, which is applied on a control volume enclosing the propeller. If the control volume surfaces are assumed to be identical to the ones used in the Wake Analysis Method in Fig. 5.1.1 and assuming steady-state, incompressible and non-cavitating flow the following surface integral equation is obtained:

$$P_{shaft} = \int_2 (\Delta p \Delta u_x + \underbrace{u_{x,1}\Delta p + \rho u_{x,1}^2 \Delta u_x + \rho u_{x,1}(\Delta u_x)^2}_{P_x} + \frac{1}{2}\rho(\Delta u_x)^2 u_{x,2})\, dA + \int_2 \left(\frac{1}{2}(u_{\theta,2}^2 + u_{r,2}^2) + \Delta\hat{e} + \Delta k\right) \rho u_{x,2}\, dA \tag{6.4.1}$$

This equation is only evaluated in the downstream Surface 2. Additionally, a pressure perturbation $\Delta p = p_2 - p_1$ and an axial velocity perturbation $\Delta u_x = u_{x,2} - u_{x,1}$ has been introduced for the sake of compactness. Here both p_1 and $u_{x,1}$ are assumed to be constant and equal to their freestream values. Three of the terms in the first surface integral constitute the thrust power P_x of the propeller. The main difference in this equation relative to the power balance equation of the Wake Analysis Method (Eq. 5.1.11) is the fact that the flow is incompressible, which allows the thrust power P_x to be identified explicitly and the entropy lost work to be set as equal to the increase in internal energy $\Delta\hat{e}$. An additional difference is the loss terms $\Delta p \Delta u_x$ and $\frac{1}{2}\rho(\Delta u_x)^2 u_{x,2}$, which represent the non-uniformity of the wake in terms of pressure and axial velocity, and will eventually be mixed out downstream of the propeller. These terms are lumped together to form a new term called the *axial wake non-uniformity loss*. The terms in the second row of Eq. 6.4.1 are also found in Eq. 5.1.11 of the Wake Analysis method, and represent swirl kinetic energy, radial kinetic energy, entropy lost work, and turbulent kinetic energy, respectively.

The energy balance method was applied on a model scale propeller for the sake of demonstration. The four-bladed propeller was simulated using STAR-CCM+ and the energy balance method was applied as a post-processing step on the control volumes A and B shown in Fig. 6.4.1 in order to also show the effect of changing the axial extent of the control volume. The resulting energy balances for the control volumes A and B are shown in 6.4.2 and display a couple of note-worthy differences. The entropy lost work has increased for the larger control volume since more of the spatial non-uniformities have

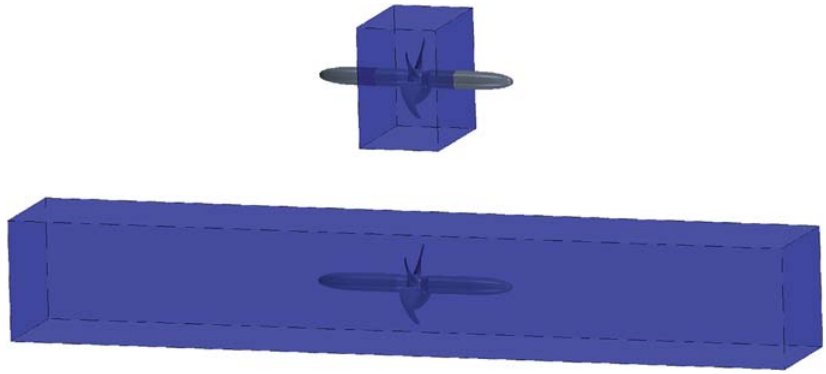

Figure 6.4.1: *Control volumes used for the evaluation of the energy balance method.*

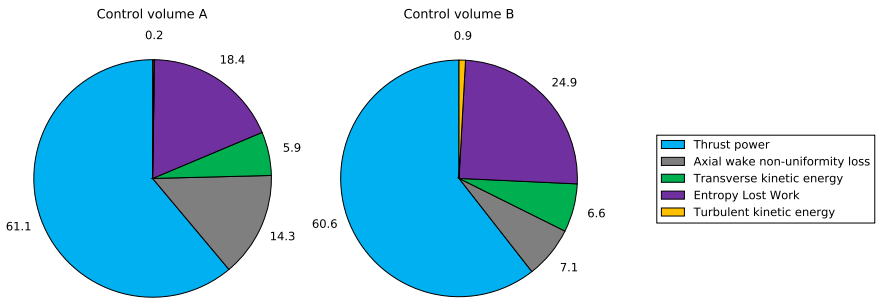

Figure 6.4.2: *The energy balance for control volumes A and B. The power levels are computed as percentages of engine shaft power. Note that the transverse kinetic energy includes both radial and swirl kinetic energy, of which latter could be partially recovered by a downstream stator or rudder.*

mixed out due to the larger axial distance. This also explains the decrease in axial wake non-uniformity loss. The transverse kinetic energy should decrease for the larger control volume, but instead it increased due to the presence of a vortex leaving the hub.

The method developed in this paper provides a clear way of breaking down the delivered shaft power into thrust power, axial wake non-uniformity losses, transverse kinetic losses, internal energy losses and turbulent kinetic energy losses. This type of analysis could be of great use for propeller and ship designers when developing new propellers or when studying propeller-ship or propeller-rudder interaction.

6.4.2 Division of work

My contribution to this paper consisted in collaborating in the development of the theory for the Energy Balance analysis due to my previous experience in developing the Wake Analysis Method for aircraft propellers. I also provided feedback and support on the results and in the writing of the paper.

6.5 Paper V

A. Capitao Patrao, T. Grönstedt, R. Avellán, and A. Lundbladh. "Wake Energy Analysis Method Applied to the Boxprop Propeller Concept", *Aerospace Science and Technology*, 2018.

6.5.1 Summary

The Wake Analysis Method presented in this paper is a further development of the one presented in Paper II. When comparing to similar existing work on the energy analysis of propellers this method removes assumptions of uniform flow, no radial flow, and constant static pressure downstream of the blade [22]. The ability to distinguish the tip vortices and wakes also sets this new method (and Paper II) apart from similar published work for the energy analysis of aircraft [56] and propellers [22]. This new version of the Wake Analysis Method is demonstrated by applying it on a conventional propeller and a Boxprop in order to highlight a number of systematic differences between the two.

The version of the Wake Analysis Method used in this paper is described in detail in chapter 5, and the major difference with respect to the earlier version in Paper II is the inclusion of the entropy lost work term ϕ_s and pressure work term ϕ_p:

$$P_{shaft} = \int_2 \left[\phi_s + \phi_p + u_{x,1}\Delta u_x + \frac{1}{2}\left((\Delta u_x)^2 + u_{r,2}^2 + u_{\theta,2}^2 \right) + (k_2 - k_1) \right] d\dot{m} \qquad (6.5.1)$$

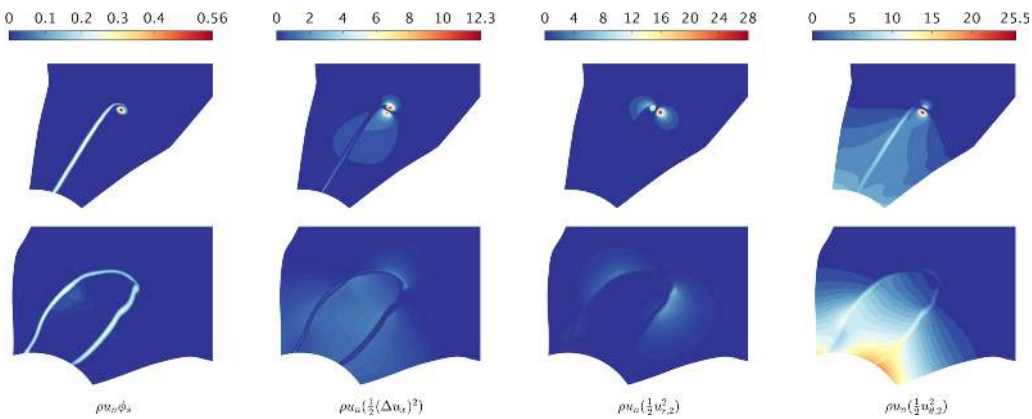

Figure 6.5.1: *Power fluxes for the loss terms of Eq. 6.5.1 for the conventional propeller (upper four plots) and the Boxprop (lower four plots). These power fluxes are evaluated on an axial plane located* $0.2D$ *downstream of the point corresponding to the propeller trailing edge at* 75% *radius.*

The different loss terms (red) and the recoverable swirl (blue) in Eq. 6.5.1 have been calculated for the GP-X-701 Boxprop and the GP-S-609 conventional propeller and are plotted in Fig. 6.5.1. The turbulent energy term has been omitted since it usually

contributes to less than 0.5% of shaft power. Here the power flux of the entropy lost work term is seen to peak at the tip vortex of the conventional propeller. For the Boxprop an increase in entropy lost work is faintly visible just above the midspan position in the blade passage. This increase is due to a passage shock at the suction side of the leading blade.

The tip vortex of the conventional propeller is visible in all plots of the conventional propeller, particularly in the radial kinetic energy subplot. For the Boxprop no circular tip vortex is seen. On the other hand, the Boxprop produces more swirl than the conventional propeller, and this is visible in the plot for the swirl kinetic power flux, where the peak values are found at the hub region of the TB.

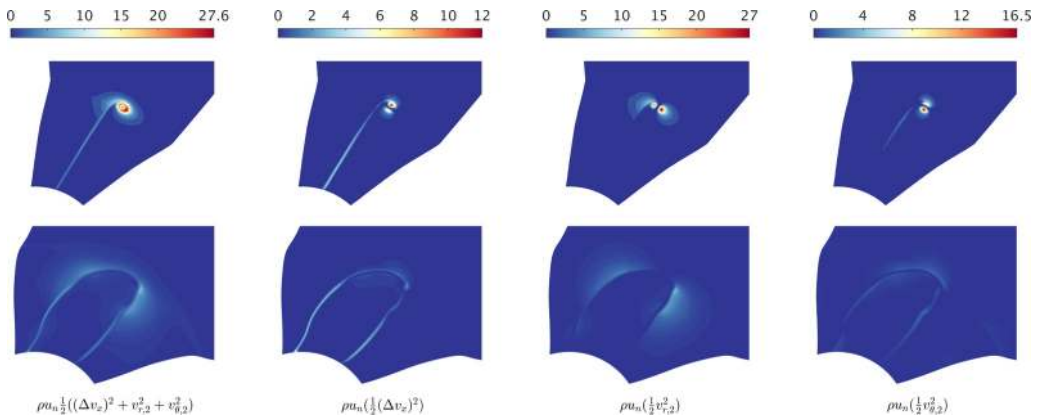

Figure 6.5.2: *Perturbation kinetic power fluxes for the conventional propeller (upper four plots) and the Boxprop (lower four plots). These power fluxes are evaluated on an axial plane located* $0.2D$ *downstream of the point corresponding to the propeller trailing edge at* 75% *radius.*

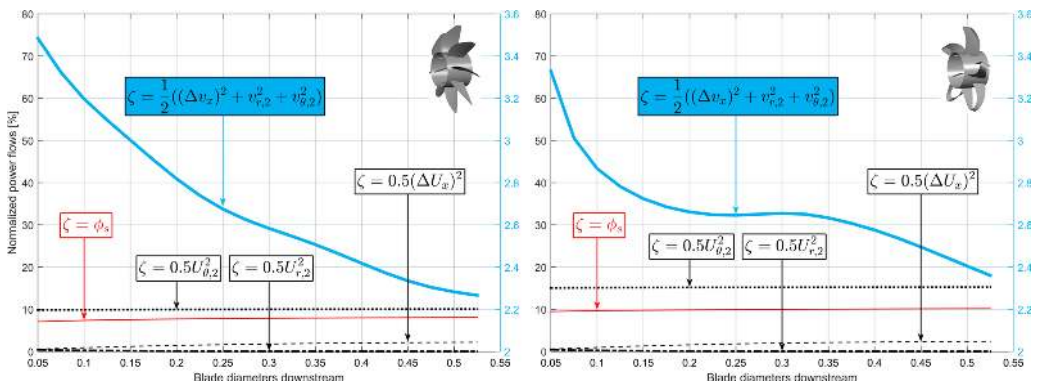

Figure 6.5.3: *Power integrals* $\int \zeta d\dot{m}$ *for the loss terms of Eq. 6.5.3 for the conventional propeller (left) and the Boxprop (right). The loss terms have been normalized with shaft power and are plotted as a function of axial distance from the propeller trailing edge (TE at 75% radius). Note that the perturbation kinetic power level is plotted on the right-hand y-axis.*

In order to better quantify the kinetic energy transferred to flow features such as tip vortices and wakes, the velocity decomposition in Eq. 5.1.12 was used. The resulting perturbation kinetic power flux is shown in Fig. 6.5.2 and indicates that for the conventional propeller most of the perturbation kinetic power flux is found in the tip vortex region. For the Boxprop, the values are significantly lower and spread out than for the conventional blade.

The power fluxes of the Wake Analysis Method can be integrated on a series of axial planes downstream of the propellers in order to visualize how the loss terms of the Wake Analysis changes with axial distance. This is shown in Fig. 6.5.3 for the Boxprop and the conventional propeller. The entropy lost work term ϕ_s increases with axial distance, as expected from the mixing out of the propeller wakes. It should be noted that most of the increase in entropy lost work has occurred when the flow passes through the blade passage. The increase that occurs in the region downstream of the blade row due to mixing is relatively small in comparison. For the swirl kinetic energy it can be seen that the power level stays relatively constant with respect to downstream distance since the hub is simulated as a free-slip surface. The perturbation kinetic energy is found to decay rapidly with increasing distance from the propellers and is of similar magnitude for both propellers. As was seen earlier, it is more concentrated to the tip vortex of the conventional blade and is more spread out for the Boxprop.

The analysis performed in this paper and in Paper II has yielded valuable insights into the magnitude of the various sources of loss found in propeller flows and how they might occur. Future optimized Boxprop designs should be analyzed in the same manner to investigate how each loss source has changed after optimization.

6.5.2 Division of work

Besides being first author, I designed both the conventional propeller and the Boxprop, performed meshing and mesh studies, performed the simulation, post-processed the results, and applied the Wake Analysis Method. I extended the Wake Analysis Method from Paper II so that it now accounts for the irreversibility of the flow, which was not possible in earlier iterations of the method. This extension of the method was prompted by a insightful question by Dr Cesare Hall of University of Cambridge at the 2016 ASME Turbo Expo conference, and secured by Tomas Grönstedt's relentless requests for iterations on the scientific content. My co-authors supervised my work and aided me in developing the Wake Analysis Method.

6.6 Paper VI

A. Capitao Patrao, D. Lindblad, A. Lundbladh, and T. Grönstedt. "Aerodynamic and Aeroacoustic Comparison of Optimized High-Speed Propellers Blades", *Joint Propulsion Conference 2018*, 7-12 July 2018, Cincinnati, OH, United States.

6.6.1 Summary

This paper strives to find the equivalency in blade count between a single-rotating Boxprop and a conventional single-rotating high-speed propeller blade by comparing their aerodynamic and acoustic performance at the cruise operating condition.

From an aerodynamic point-of-view only, and for a given propeller activity factor, a propeller should feature as many blades as possible, since this increases its induced efficiency. From a structural mechanics point-of-view, a high number of thin blades with low chord values would lead to high blade stresses and an increased risk for flutter [21]. For the Boxprop, there is an additional limit set by the space required by the blade pitching mechanism compared to a conventional blade. Moreover, a Boxprop with B number of Boxprop blades can be argued to have either B or $2B$ propeller blades, depending on if the leading and trailing blades are seen as two separate blades, or as one single blade.

Three types of propellers were optimized in this paper for maximum propeller efficiency and thrust: 1) a 6-bladed Boxprop, 2) a 6-blade conventional propeller blade, and a 3) 12-bladed conventional propeller. The propellers have a diameter of 4.2672 m and operate at the cruise operating point with an axial Mach number of 0.75 and a flight altitude of 10668 m. Compared to Paper III the number of design variables used for the Boxprop has increased from 17 to 32, and these design parameters are described in Section 2.2.2. After the optimization three designs were chosen, one from each propeller type, with a thrust coefficient $C_T = 0.375$, which is representative of the thrust coefficient found on the front rotor of modern CRORs. These three designs were then re-simulated with larger computational domains and finer meshes for further aerodynamic and acoustic analysis. The noise signature produced by the propellers was obtained by solving the convective form of the Ffowcs Williams - Hawkings equations for permeable sampling surfaces [57]. A description of the acoustic methodology used in this paper can be found in [58].

The performance of the three chosen propellers indicate that the propeller efficiency of the Boxprop lies in-between its 6-bladed and 12-bladed counterparts, as is shown in Fig. 6.6.1. This is also evident when analyzing the blade sectional thrust, which is shown in Fig. 6.6.2 together with the sectional lift and lift-to-drag ratios for all three designs. The location of peak thrust of the Boxprop lies between the 12-bladed and the 6-bladed conventional propellers. The 12-bladed propeller produces thrust further out radially when compared to the 6-bladed due to its higher aspect ratio, while the Boxprop produces less thrust at the tip due to its arc-shaped tip. At the absolute tip of the Boxprop the lift vector is parallel with the radial direction yielding no contribution from lift to thrust. Instead the only contribution comes from drag, which results in negative thrust at the tip for the Boxprop. Another major difference is the lift-to-drag ratios of the Boxprop, whose values match the ones for the conventional propellers from 50% to 80% of the tip radius. Outside this area the Boxprop lift-to-drag ratio is seen to decrease.

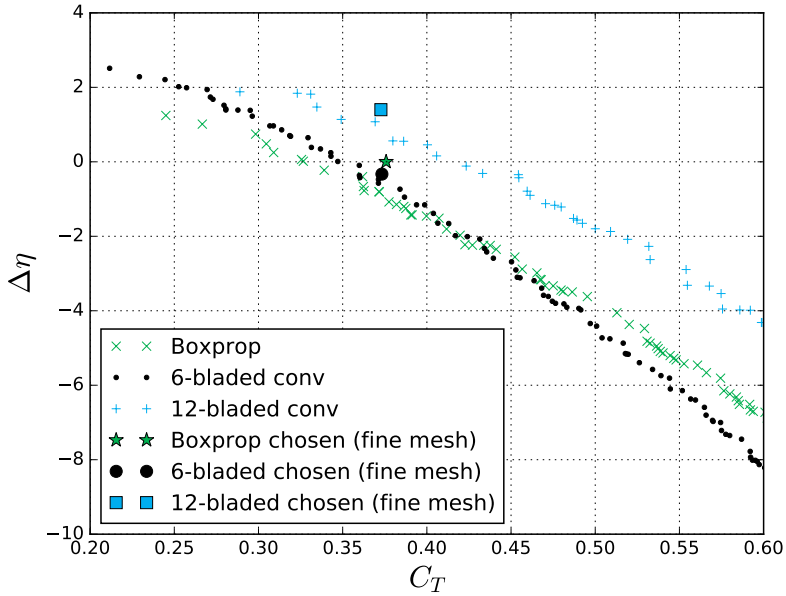

Figure 6.6.1: *Values of thrust coefficient and propeller efficiency for the optimization of the Boxprop, the 6-bladed conventional propeller, and the 12-bladed conventional propeller. The Pareto fronts of all three optimizations have been plotted together with the results of the three re-simulated propellers with $C_T = 0.375$ and finer meshes. The propeller efficiencies have been subtracted by the propeller efficiency of the re-simulated Boxprop.*

When analyzing the flow downstream of the propeller blades a vortex-like structure appeared in the wake of the Boxprop, albeit significantly weaker than the tip vortices found for the conventional blades. This is illustrated in Fig. 6.6.3 which shows that the peak vorticity magnitude of the Boxprop is 32% weaker than the 6-bladed conventional blade and 20% weaker than the 12-bladed one.

With regards to the optimization process itself it was found that the process is more challenging for the Boxprop than for a conventional blade for several reasons:

- The higher number of design variables required for the Boxprop (32 versus 20). This increases the dimensionality of the search space.
- The lack of a decent initial guess or baseline design for the Boxprop. Presently, there is no analytical method for producing minimum-induced loss Boxprop designs, which necessitates the use of 3D CFD and optimization.
- The performance of the Boxprop blade halves is coupled - This was seen by varying the angle-of-attack distribution of the LB and TB separately. Changes in the TB angle-of-attack distribution affected the performance of both the TB and LB, while changing the LB angle-of-attack distribution only affects the LB itself.

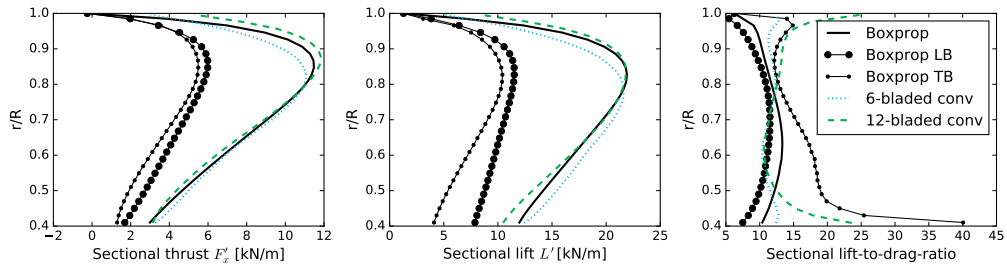

Figure 6.6.2: *Sectional performance of the three optimized propellers.*

The noise levels for these single-rotating propellers were computed for a set of near-field and far-field observers. The near-field observers were located on circular arcs with a radius of $2D$ while the far-field observers were located at $10D$. All three propellers showed similar noise directivities but slightly different noise levels, which were found to rank according to their propeller efficiency. It was found that the lowest noise level was produced by the 12-bladed conventional propeller, followed by the Boxprop. The 6-bladed conventional propeller produced most noise. For an equal-thrust propeller a lower efficiency results in higher disk loading and therefore higher blade forces, which produces more noise.

The main conclusion of this paper is that the aerodynamic and acoustic performance of 6-bladed Boxprop lies somewhat in-between its 6 and 12-bladed conventional counterparts. The main hypothesis of the Boxprop is to reduce the tip vortex strength compared to a conventional propeller, thereby minimizing the interaction noise when incorporating it into a CROR. Whether this is the case at the take-off operating conditions remains to be investigated in the future.

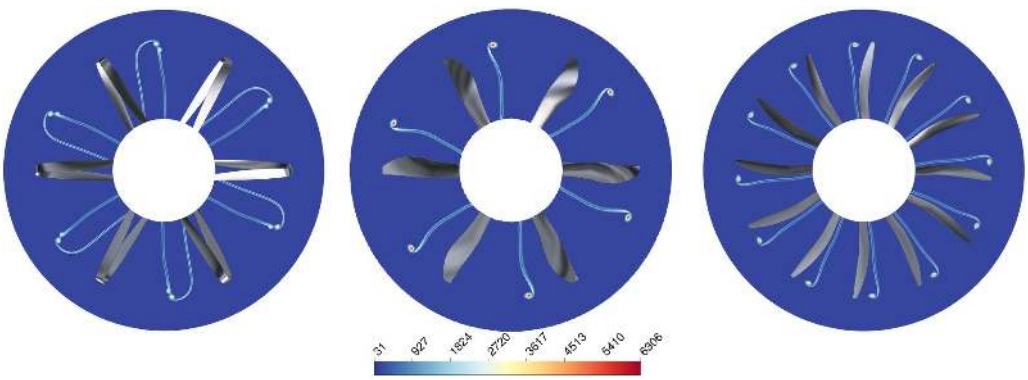

Figure 6.6.3: *Vorticity magnitude [1/s] for the 6-bladed Boxprop (left), the 6-bladed (center), and the 12-bladed conventional propeller (right) on planes at a distance of* $0.2D$ *from the trailing edges of the 75% radial position of the blades.*

6.6.2 Division of work

Besides being the first author, I performed the optimizations of the three propeller types, created the finer meshes for the re-simulated cases, and performed the aerodynamic analysis. Daniel performed the acoustic post-processing and analysis of the three propellers and wrote the sections of the paper relating to acoustics.

6.7 Paper VII

A. Capitao Patrao, T. Grönstedt, A. Lundbladh, and G. Montero Villar. "Wake Analysis of an Aerodynamically Optimized Boxprop High Speed Propeller", *Submitted to Journal of Turbomachinery on the 16th of August 2018.*

6.7.1 Summary

Early Boxprop designs experienced significant interference effects between the blade halves, leading to higher amounts of swirl and lower propeller efficiency than conventional equal-thrust propellers. This was seen in Paper V using the Wake Analysis Method, and in this paper the method is applied to an aerodynamically optimized Boxprop in order to investigate how the losses have changed after the optimization and how the optimized Boxprop compares with optimized conventional propellers. The optimization aims at maximizing thrust and propeller efficiency and is carried out on a full-scale, 6-bladed Boxprop at the cruise operating condition with a diameter of 4.2672 m and a freestream Mach number of 0.75. Relative to the optimization performed in Paper III the number of design parameters has been increased to 32 in order to include both blade section camber and chord. The stacking line is still kept as mirror-symmetric in order to keep down the number of design variables and for providing a balanced mechanical layout.

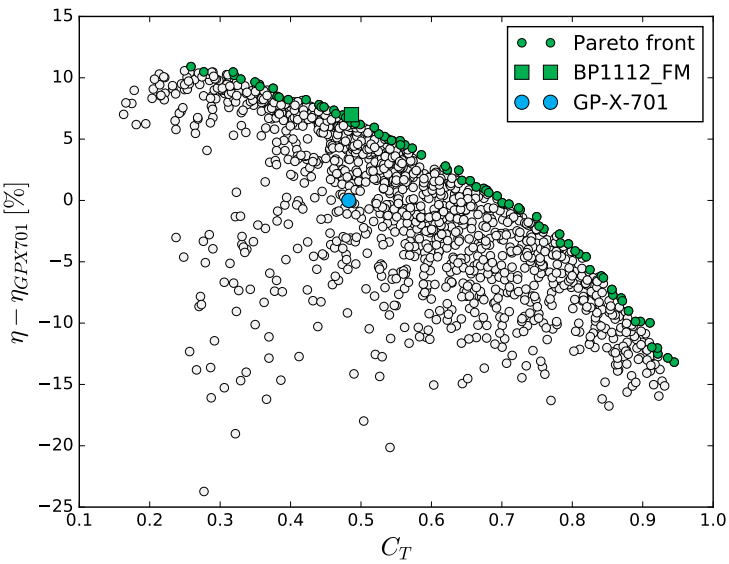

Figure 6.7.1: *Results for the aerodynamic optimization of a 6-bladed Boxprop, Pareto front shown in green. The BP1112 design from the Pareto front with a thrust coefficient close to the GP-X-701 has been re-simulated with a finer mesh (BP1112_FM). Note that the propeller efficiencies have been subtracted with the propeller efficiency of the GP-X-701.*

The optimization yielded performance results from CFD for 1452 Boxprop designs, which are shown in Fig. 6.7.1. Here the propeller efficiency has been subtracted by the efficiency of a scaled-up version of the older GP-X-701 Boxprop (from now on referred to as legacy), yielding a 7% percentage point improvement in propeller efficiency for the optimized BP1112 design with $C_T = 0.486$. Even larger improvements in efficiency have been achieved for lower levels of thrust.

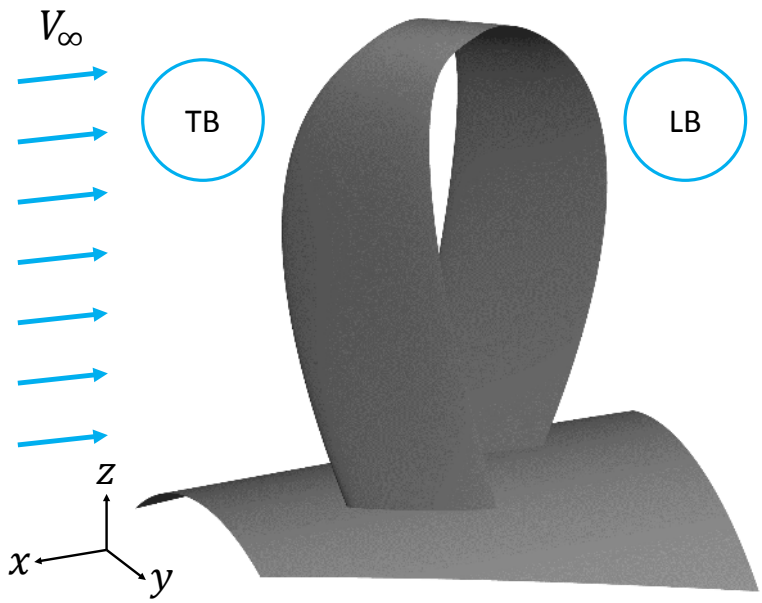

Figure 6.7.2: *The chosen Boxprop BP1112 from the Pareto front of the optimization. The rotational axis lies in the direction of the x-axis.*

The chosen BP1112 Boxprop design features blade halves swept in opposite directions, the LB being swept downstream, and the TB being swept upstream, as is shown in Fig. 6.7.2. This is a common design trait found in all optimal Boxprop designs in the Pareto front of the optimization since it decreases blade interference and allows each blade half to produce thrust at high radii - where it results in the least amount of swirl. This design trait is visualized in Fig. 6.7.3 for all the cases in the Pareto front. Another method for visualizing this is by calculating a chord displacement angle distribution $\kappa(r)$ for the stacking line, using the same approach as was used to construct the stacking line control points P_i in Fig. 2.2.1, but backwards. Instead of specifying κ_i and d_i to get the coordinates of the control point P_i, we specify the coordinates of each stacking line point and obtain the chord displacement angle distribution $\kappa(r)$ for the stacking line. This distribution is plotted in Fig. 6.7.4 for all the cases in the Pareto front. As can be seen $\kappa(r)$ ranges from rougly 35° to 40° at $r/R = 0.75$, with an average of 41°.

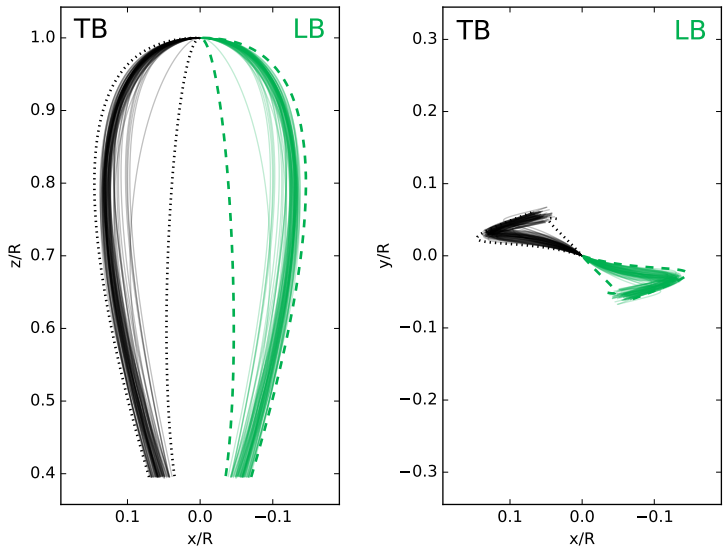

Figure 6.7.3: *LB (solid green) and TB (solid black) stacking lines for all the cases in the Pareto front of the optimization. The dashed lines are the limits in stacking line positions for the LB (green) and TB (black) resulting from using the min/max values of the chord displacement angle κ_i and blade passage distance d_i. Note the flipped x-axis, in order to be consistent with previous Boxprop images where the undisturbed flow goes from left to right.*

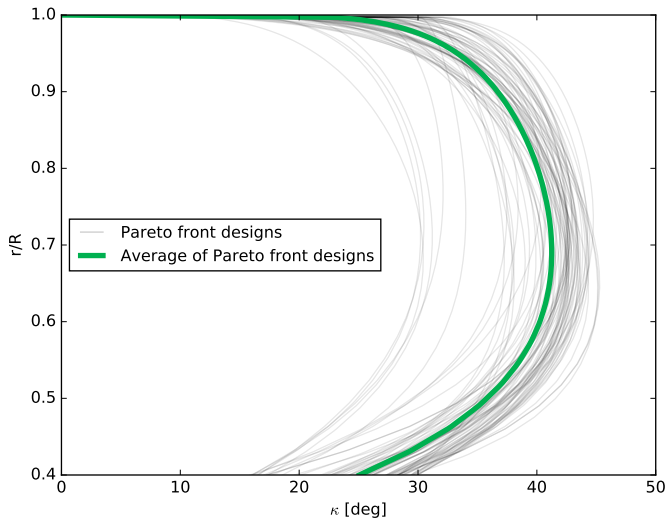

Figure 6.7.4: *Calculated displacement angle $\kappa(r)$ distribution for each coordinate of the stacking line. Curves in grey denote the displacement angle distributions of each individual Pareto front design while the green line denotes the average of the entire Pareto front.*

The Wake Analysis Method from Chapter 5 was used to investigate how the losses have changed after optimization and how well the Boxprop compares to the optimized conventional propellers. Four propellers were analyzed; the optimized BP1112, the legacy GP-X-701 Boxprop, a 6-bladed conventional propeller, and a 12-bladed conventional propeller. The loss terms of the Wake Analysis in Eq. 5.1.14 have been calculated and plotted in Fig. 6.7.5. Here it can be seen that relative to the legacy GP-X-701 Boxprop, the optimized BP1112 Boxprop features significantly lower amounts of entropy lost work and swirl in the wake. The optimized Boxprop also experiences lower Mach numbers and therefore weaker shocks on the suction sides of the blade, which decreases the amount of entropy lost work relative to the legacy design. As was mentioned earlier, the lower amount of swirl is due to lower blade interference at high radii. The perturbation kinetic energy is slightly higher for the optimized Boxprop due a new vortex-like structure emanating from the blade, something which was not found in the legacy GP-X-701. Relative to the optimized conventional propellers, the magnitude of the losses of the 6-bladed BP1112 lies somewhere between its 6 and 12-bladed conventional counterparts. It produces similar amounts of entropy lost work as the 12-bladed propeller, but higher than the 6-bladed one due to weaker shocks at the tip of the optimized 6-bladed conventional propeller.

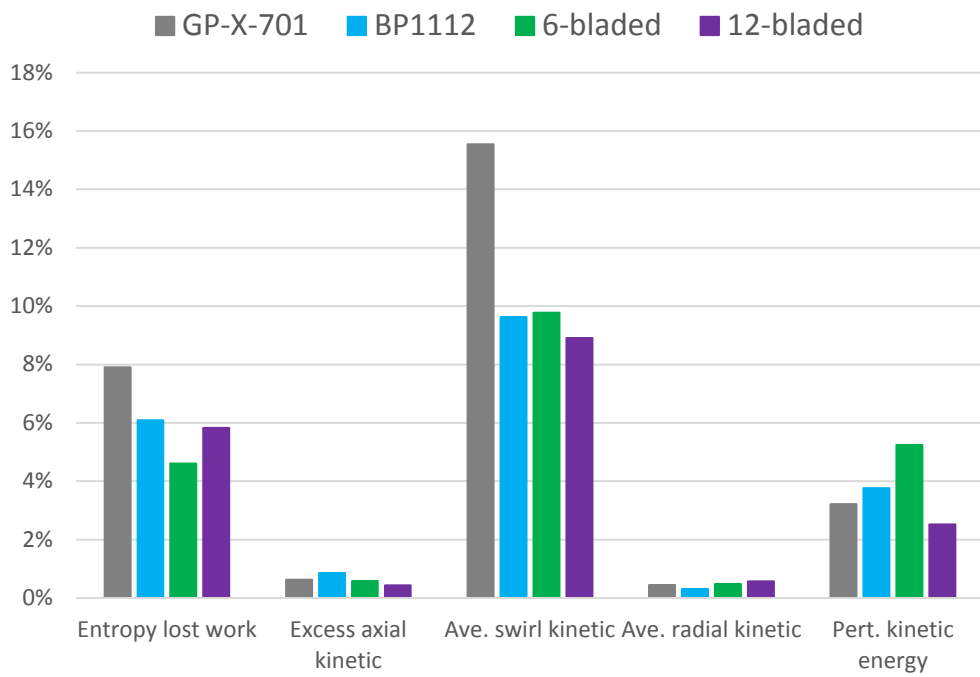

Figure 6.7.5: *The magnitudes of the various loss sources for the propellers. The losses are presented as percentages of the engine shaft power for each propeller.*

The optimized BP1112 Boxprop produces a vortex-like structure from its tip region as shown in Fig. 6.7.6 and 6.7.7, and there are two major differences versus the tip vortices found in the optimized conventional propellers. The first is that the peak vorticity of the vortex from the Boxprop is considerably lower than for the conventional propellers. At $0.2D$ downstream of the blades, as shown in Fig. 6.7.6, the peak vorticity level of the Boxprop is 50% and 46% lower than the levels in the tip vortices of the 6 and 12-bladed conventional propellers, respectively. The second major difference lies in how the vortices form and how they develop for the two types of propellers, as is shown in Fig. 6.7.7. Here it can be seen that the Boxprop vortex is a result of the wake rolling up on itself with the vortex streamlines originating from a broad area around the blade arch tip, which then coalesce into a more compact vortex. By contrast, the tip vortex of the conventional blade is formed in a relatively small region at the blade tip.

The acoustic impact of the Boxprop vortex during take-off conditions cannot be evaluated at this stage, as it would require additional simulations to verify its existence at take-off conditions together with an appropriate acoustic analogy. At this point, it can only be noted that at cruise conditions the optimized Boxprop BP1112 features higher wake vorticity levels than the legacy GP-X-701, but substantially lower than what is present in the tip vortex of both the optimized 6 and 12-bladed conventional propellers.

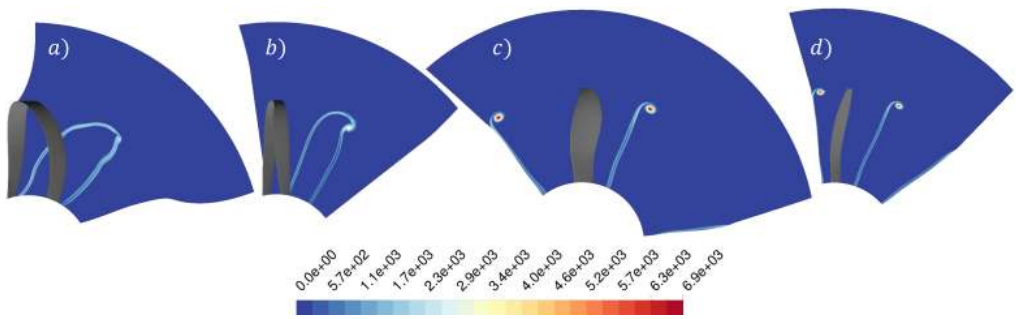

Figure 6.7.6: *Vorticity contour plots at* $0.2D$ *downstream of the* 75% *radial position of the a) legacy GP-X-701 Boxprop, b) optimized BB1112 Boxprop, c) optimized 6-bladed conventional propeller, and d) optimized 12-bladed conventional propeller.*

6.7.2 Division of work

Besides being the first author, I performed the optimizations of all the analyzed propellers, created the finer meshes needed for the cases analyzed with the Wake Analysis Method, and performed the aerodynamic analysis. As in Paper III, Gonzalo was instrumental in the optimization effort of the propellers in this paper. My co-authors also supervised my work and provided feedback on the writing of the paper.

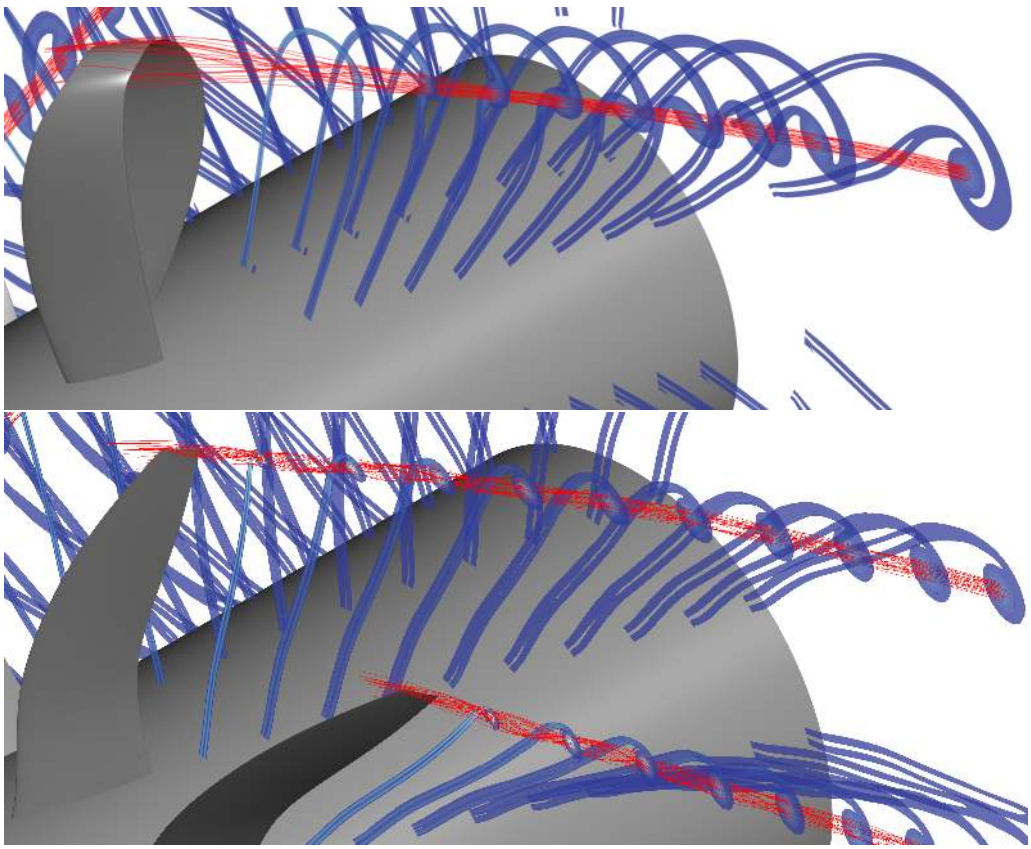

Figure 6.7.7: *Axial cuts of wake vorticity (blue) and vortex streamlines (red) for the BP1112 (upper image) and the optimized 12-bladed conventional propeller (lower image). The axial cuts range downstream axial distances of* $0.05D$ *to* $0.525D$ *from the 75% radial position of the blade trailing edge.*

6.8 Other relevant publications

6.8.1 Paper VIII

A. Capitao Patrao, "Implementation of Blade Element Momentum/Vortex Methods for the Design of Aero Engine Propellers," Tech. rep., 2017:06.

Summary

This internal report outlines the theory and methodology used in the Chalmers in-house propeller design code OPTOPROP. This design code was developed in order to enable the design of propeller blades for aircraft engines, particularly for open rotors, both single and counter-rotating.

A literature study was performed in order to find suitable propeller design and analysis methods. A number of promising methods based on the Blade Element-Momentum/Vortex methods [33, 34, 40] were implemented. Additionally, an in-house variant of these design and analysis methods was derived which could account for non-uniform propeller inflow.

The implemented methods were validated for the case of single-rotating propellers against experimental results from literature [59, 60] and numerical (CFD) simulations and show good accordance in the trends of the performance values. The design methods would benefit from calibration since the obtained thrust values from CFD are slightly under-predicted relative to the values specified in OPTOPROP. Nevertheless, the design program has shown itself to be very useful for the design of propellers and open rotor blades, especially for the design of baseline blades for further optimization using CFD.

6.8.2 Paper IX

V. Tavares Silva, L. Moraes da Silva, J. Takachi Tomita, C. Bringhenti, T. Grönstedt, A. Capitao Patrao, and O. Petit, 2017, "Numerical Simulation of Nacelle Flowfield for Counter-Rotating Open Rotor Propellers", *23rd ISABE Conference*, September 3–8, Manchester, United Kingdom.

Summary

This conference paper presents results on the preliminary design of axisymmetric nacelles for counter-rotating open rotors. A nacelle design code developed in Matlab is presented and demonstrated by designing an open rotor nacelle. Design and operating point parameters for the nacelle have been chosen to match the ones used by Negulescu [21], namely a front rotor diameter of $4.2672\,m$, a hub-to-tip ratio of 0.35, a flight altitude of $10668\,m$, and a cruise Mach number of 0.75. CFD simulations were performed for this nacelle at a range of angles-of-attack from 2° to 8°. The CFD results of the nacelle design showed no aerodynamic issues which could otherwise have affected the aerodynamic performance of the engine, namely no major boundary layer thickening, and no shock waves in neither the cowl nor the in the inlet.

My contribution in this paper was in co-developing the nacelle design code during my research visit to Instituto Tecnológico de Aeronáutica (ITA) in 2015. I also provided feedback on the CFD results and in the writing of the paper.

6.8.3 Paper X

Lindblad, D., Montero Villar, G., Andersson, N., Capitao Patrao, A., Courty-Audren, S. K., and Napias, G. (2018). "Aeroacoustic Analysis of a Counter Rotating Open Rotor based on the Harmonic Balance Method". *In 2018 AIAA Aerospace Sciences Meeting*, (p. 1004).

Summary

This paper presents a Computational Aeroacoustics (CAA) platform for the noise estimation of counter-rotating open rotors. The noise signature of the open rotor is obtained by simulating the flow using the Harmonic Balance method and post-processing the solution with a Ffowcs Williams-Hawkings (FW-H) acoustic analogy. The methodology is demonstrated on a full scale ($D = 4.2672\,m$), generic counter-rotating open rotor at the cruise operating condition. My main contributions to this paper included the aerodynamic design of the propeller blades using the in-house propeller design tool OPTOPROP and providing feedback regarding the aerodynamic results and the writing of the paper.

7 Unpublished Results

The aim of this chapter is to present some of key results that have been obtained during the research project, but which have not been published yet.

7.1 The Boxprop Counter-Rotating Open Rotor

7.1.1 Initial design

The ultimate goal of this research project is to incorporate the Boxprop as the front rotor of a CROR and investigate if it can decrease interaction noise at take-off conditions by surpressing or eliminating its tip vortex. One step on the journey to that goal is to investigate whether this CROR configuration is competitive or not at the cruise operating point. For it to be competitive it needs to deliver sufficient thrust at a similar propeller efficiency as other published CROR designs. The comparison can also be done using the Wake Analysis Method in order to compare the magnitude of the aerodynamic losses in the flow.

There is not a great deal of data published on the propeller efficiency achieved by modern CROR's, but there are two papers that should be mentioned. The first is a 2013 paper by Negulescu [21] which provides a detailed description of the propeller blade design process for open rotors together with thrust and propeller efficiency targets for the Airbus AI-PX7 CROR at cruise and take-off conditions. The second paper is the 2014 paper by Hall [22] which provides the propeller efficiency and loss composition for a 1980's CROR design (Rolls-Royce Rig-140) and a more recent design from 2012 (Rolls-Royce Rig-145). Losses such as entropy lost work and swirl kinetic energy are included in an analysis similar to the Wake Analysis, but unfortunately the thrust levels for neither open rotor is included, thereby preventing a strict comparison on an equal-thrust basis. Instead, the levels of loss should be seen as rough indicators to which the Boxprop can be compared. The thrust of the Rolls-Royce Rig-140 has been estimated using the performance data given by Zachariadis [61], and is included in Table 7.1.3.

Table 7.1.1: *Operating point, operating conditions, and performance targets for the BPOR.*

Operating point	Operating conditions	Target thrust	Target η
Cruise	Mach 0.75, 10668 m, ISA+0K	18905 N	$85\% \pm 1\%$
Take-off	Mach 0.2, sea level, ISA+15K	107775 N	60%

The performance targets set for the **B**ox**p**rop counter-rotating **O**pen **R**otor (BPOR) are derived from the ones used by Negulescu [21] and are presented in Table 7.1.1. The main design parameters for the BPOR are shown in Table 7.1.2. The front rotor diameter and rear rotor clipping are chosen to be identical to the AI-PX7 CROR, as is the torque split, and rotational speed at take-off. The Boxprop which operates as the front rotor of the BPOR has 6 blades, since it can be considered to have either 6 or 12 blades depending on if both individual blade halves are being considered or the entire Boxprop blade. The

Table 7.1.2: *Main design parameters and performance of the BPOR. Note that the thrust and propeller efficiency account for the drag and torque on the rotating hub surfaces of the propeller blades.*

Front number of blades B_{FR}	6
Rear number of blades B_{RR}	11
Front rotor diameter $D\,[m]$	4.2672
Rear rotor clipping $[m]$	$0.1D$
HTR	0.4
Intra-rotor spacing $[m]$	$0.27D$
Rotational speed at cruise $[rpm]$	878.4
Rotational speed at take-off $[rpm]$	1032
Airfoil family	NACA16
Front/rear rotor torque split at cruise	54.8/45.2
Thrust at cruise $[N]$	19172
Propeller efficiency at cruise	83.20%

HTR and cruise rotational speed are different compared to the AI-PX7 in order for it to be consistent with previous Boxprop design work. The intra-rotor spacing is higher than for the AI-PX7 CROR ($0.27D$ vs $0.22D$) but still within the range recommended by Negulescu. A higher value of the intra-rotor spacing is also common in other open rotor designs [20, 22, 62].

The BPOR is designed according to the steps outlined in Chapter 2.4, yielding the cruise and take-off performance values shown in Table 7.1.2. As can be seen, the required thrust level at cruise is reached, but the propeller efficiency is slightly below the target. It should be noted that the propeller efficiency reaches 84.69% while meeting the thrust target if the rotating hub surface is excluded and only the blade surfaces are used when calculating the propeller efficiency. This is important to consider since the paper by Negulescu [21] does not state whether the rotating hub surfaces are included or not when calculating the propeller efficiency. Nevertheless the aerodynamic performance of the BPOR at cruise is seen as satisfactory, even though there is room for improvement.

The geometry of the BPOR is shown in Fig. 7.1.1 together with Mach number contours of the supersonic regions of the flow. As can been, the Mach numbers are relatively low for the Boxprop, while the rear blade seems to be more highly loaded due to the higher Mach numbers and more extensive supersonic regions. The main reason for the high loading of the rear blading can be attributed to its clipping, which increases its thrust coefficient C_T by 52% compared to an equal-thrust, non-clipped rear blade. The high Mach number regions in the rear blade are also partially the result of it being an analytically derived design. If it were to be optimized in the same manner as the front rotor, the Mach numbers, and consequently the shock losses, should decrease. From Fig. 7.1.1 it can also be seen that the Boxprop has no problems with blade interference - especially compared to the flow of the GP-X-701 in Fig. 6.2.2.

For the take-off operating point the front and rear rotor blades needed to be re-pitched (rotated) in order to better match the incoming flow and to deliver the target thrust. It quickly became evident that the current BPOR geometry had simulation convergence

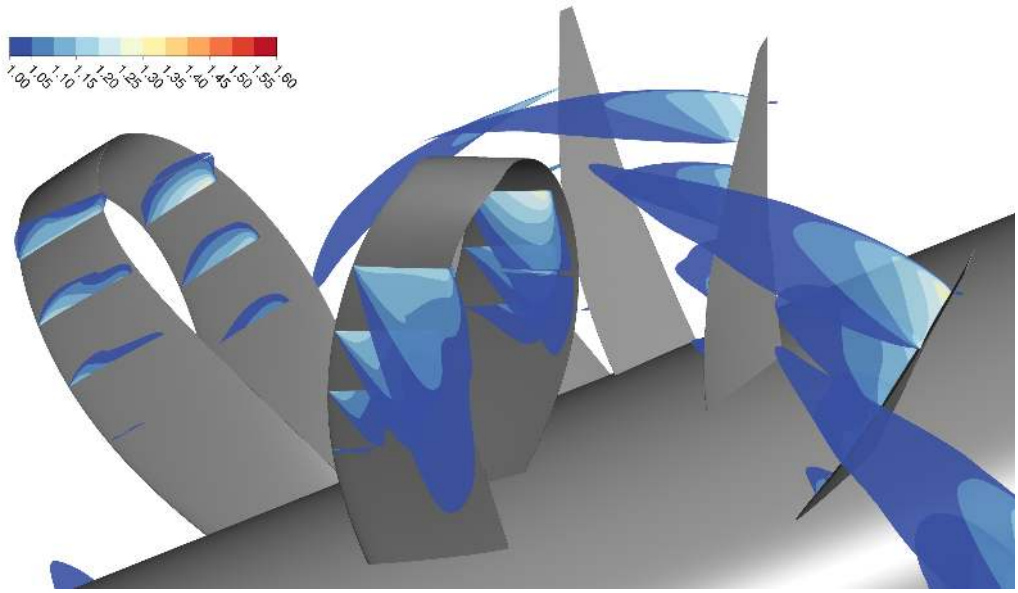

Figure 7.1.1: *Mach number contours at different radii (rotating frame of reference). Note that the maximum Mach numbers occur at the leading edge of the rear rotor.*

issues for the take-off operating point and could not deliver the required levels of thrust according to Table 7.1.1 without excessive flow separation and low propeller efficiency. The blade chord, camber, and even rotational speed would need to be increased in order to obtain better performance at the take-off operating point. In essence, a well designed CROR needs to be a trade-off between maximizing efficiency at cruise and delivering enough thrust at take-off.

7.1.2 Design optimized for cruise

In order to investigate further possible gains in propeller efficiency at cruise the BPOR design was optimized using the parametrization in Chapter 2 and the optimization methodology presented in Chapter 4. The full parametrization of the BPOR contains 52 design parameters for optimization, which would require 1431 CFD simulations for the LHS alone, almost three times as many as the CFD simulations in the LHS of the Boxprop optimization performed in Paper VII. Since the Boxprop of the BPOR had already been optimized on its own, it was decided to reduce the number of design variables by keeping its stacking line fixed. It was seen in paper VII that that all optimal propeller designs featured blade halves swept in opposite directions, so this reduction in design parameters should not result in any major performance penalty.
The aerodynamic optimization of the full BPOR resulted in 3249 CFD simulations. From this optimization, a BPOR design with the required thrust level and torque ratio was chosen. Its performance is shown in Table 7.1.3 together with performance data for other

Table 7.1.3: *Blade counts, thrust level, propeller efficiency, entropy lost work for the front and rear rotor, and the swirl kinetic energy downstream of the rear rotor for various CROR models. Note that the entropy lost work and swirl kinetic energy have been normalized with the shaft power of the CROR. The propeller efficiencies in parentheses are calculated using only the blade thrust and torque, excluding the hubs. The thrust level of Rig-140 has been estimated by scaling its thrust from rig-scale (D=0.76m) to full-scale (D=4.2672m). Efficiency and losses have not been scaled.*

CROR	D	B_{FR}xB_{RR}	F_x [kN]	η	$\phi_{s,FR}$	$\phi_{s,RR}$	$\frac{1}{2}u_\theta^2\dot{m}$
Rig-140	0.76m	7x7	13.2	83%	5.5%	6%	0.8%
Rig-145	N/A	12x9	N/A	86%	4.8%	4.4%	0.9%
AI-PX7	4.27m	11x9	21.1	84%	N/A	N/A	N/A
BPOR	4.27m	6x11	19.2	83.2% (84.7%)	6.47%	7.03%	0.87%
BPOR-opti	4.27m	6x11	19.5	84.2% (86.0%)	6.69%	5.72%	0.48%

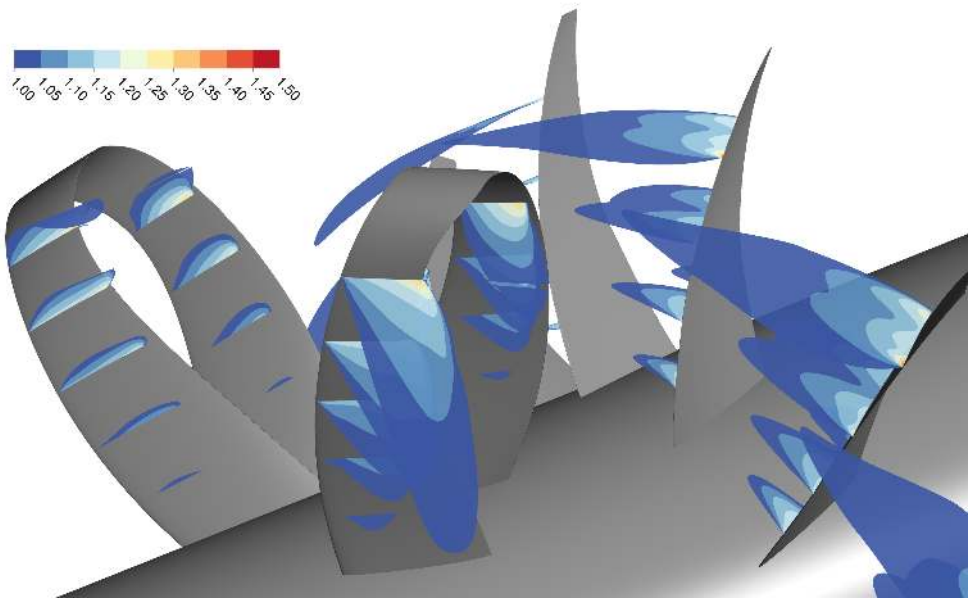

Figure 7.1.2: *Mach number contours at different radii (rotating frame of reference) for the optimized BPOR.*

publised CROR designs. Here it can be seen that the propeller effiency of the BPOR has been improved by reducing the overall amount of entropy lost work and downstream swirl. The decrease in entropy lost work is also in line with the lower Mach numbers, weaker shocks, and smaller regions of supersonic flow of the optimized BPOR in Fig. 7.1.2.

To conclude, BPOR performance at cruise is competitive with regards to other publised CROR designs, and poses no problem in terms of aerodynamic performance at cruise.

8 Concluding Remarks

The results contained in this thesis constitute steps towards the final goal of ascertaining whether a CROR incorporating a Boxprop can operate efficiently and with lower levels of interaction noise than existing CRORs. The finish line has not yet been reached since there is some work remaining regarding performance and acoustics at take-off, but it is within sight. However, there are many useful insights and conclusions that can be drawn from the work presented in this thesis:

- Performance results from CFD show good agreement with experiments for the take-off operating point, thereby increasing confidence in the computational methods. Including surface roughness and blade deformation in the CFD simulations was important since the experiments featured 3D-printed plastic propellers.

- Early Boxprop designs such as the GP-X-701 encountered significant amounts of interference between the blades, illustrated in Fig. 8.1.1. The interference prevented the Boxprop designs from producing thrust at high radii since a low pressure/high Mach number area formed in the blade passage, leading to lower amounts of thrust on the TB and higher amounts of swirl. The interference also led to different angles-of-attack for the LB and TB, which needs to be accounted for in the design phase of the propeller.

- A Wake Analysis Method has been derived in order to provide a detailed breakdown and quantification of the aerodynamic losses in flow. It is also able to distinguish and quantify the kinetic energy in the tip vortices and blade wakes. For the GP-X-701, the two largest sources of loss were swirl and entropy lost work, which prompted new ideas on how to shape the Boxprop for improved efficiency. The Wake Analysis Method showed similar magnitudes in the kinetic energy of the tip vortices and wakes for the Boxprop and an equal-thrust conventional blade. It could also be seen that the kinetic energy was more spread out for the Boxprop, with no evidence of a tip vortex in the flow.

- The three-dimensional shape of the Boxprop renders classic propeller design methods ineffective. Instead it was chosen to develop an optimization platform which incorporated the use of GAs and CFD. The geometric parametrization and the optimization framework described in this thesis have been successful at finding new aerodynamically optimized Boxprop designs. These designs have managed to increase propeller efficiency significantly by reducing entropy lost work and swirl losses. For the same thrust coefficient as the legacy GP-X-701 Boxprop the propeller efficiency has increased by 7 percentage points.

- A key geometric feature found on all optimized Boxprop geometries is the sweeping of the LB and TB in opposite directions, which decreases blade interference and generated swirl.

- The optimized Boxprop blades manage to produce thrust at higher radii compared to older designs. This radial shift has decreased the amounts of generated swirl,

but has also resulted in the formation of a vortex-like structure downstream of the Boxprop. Compared to the tip vortex of conventional propeller blades there are two major differences:

1. The Boxprop vortex is a result of the wake rolling up on itself with the vortex streamlines originating from a broad area around the blade arch tip, which then coalesce into a more compact vortex. For a conventional propeller, the tip vortex forms in a relatively small region at the blade tip.
2. The vorticity magnitude of the Boxprop vortex has been observed to be lower than the tip vortex of the conventional propeller blade.

Achieving thrust at higher radii is a consequence of sweeping the LB and TB in opposite directions. This suggests that the sweeping of the blade halves could potentially allow the designer to trade tip vortex strength for aerodynamic performance. In should be noted that the Boxprop vortex was found at the cruise operating point, and future research should investigate the existence and acoustic impact of this vortex at the take-off operating point.

- The aerodynamic performance and the noise level of a single-rotating, 6-bladed Boxprop at the cruise operating point was found to be better than a equal-bladed conventional propeller, but worse than a conventional propeller with twice as many blades. The noise level ranks with efficiency since higher efficiency entails lower blade torque, lower blade loading, and therefore lower loading noise.

- Optimizing a Boxprop was found to be more challenging than a conventional propeller due to more design parameters, no methods for performing initial design of the Boxprop, and the coupled nature of the performance of the Boxprop blade halves (interference).

- A CROR featuring a Boxprop as its front rotor (BPOR) has been shown to be able to operate efficiently and deliver the required thrust at cruise, showing competitive levels of performance compared to other published CROR designs.

8.1 Future work

- Tailoring and optimization of the tip of the Boxprop could potentially unlock new abilities to shape the flow downstream of the propeller by varying the angle-of-attack, camber and thickness of the tip profile. The optimizations presented in this thesis have been carried out with a tip profile with zero angle-of-attack and camber in order to decrease the amount of design variables and computational cost.

- Further improvements in efficiency should be obtainable by unlocking more design parameters during optimization and allowing for different rotational speeds, asymmetrical stacking lines, asymmetrical chord distributions, and fully parametrized airfoils.

- High efficiency for the BPOR at take-off conditions is required to remain competitive with other published open rotors. A well-designed CROR is a trade-off between achieving high efficiency at cruise and delivering the required thrust at take-off. Therefore, ongoing and future work should attempt to produce new designs with more blade area, camber, and higher rotational speed at take-off without compromising efficiency at cruise.
- The noise level at the take-off operating point is instrumental for the future fate of the Boxprop. Once a BPOR is designed which can operate efficiently at take-off conditions, its acoustic signature needs to be investigated, including the existence and acoustic impact of the Boxprop vortex.

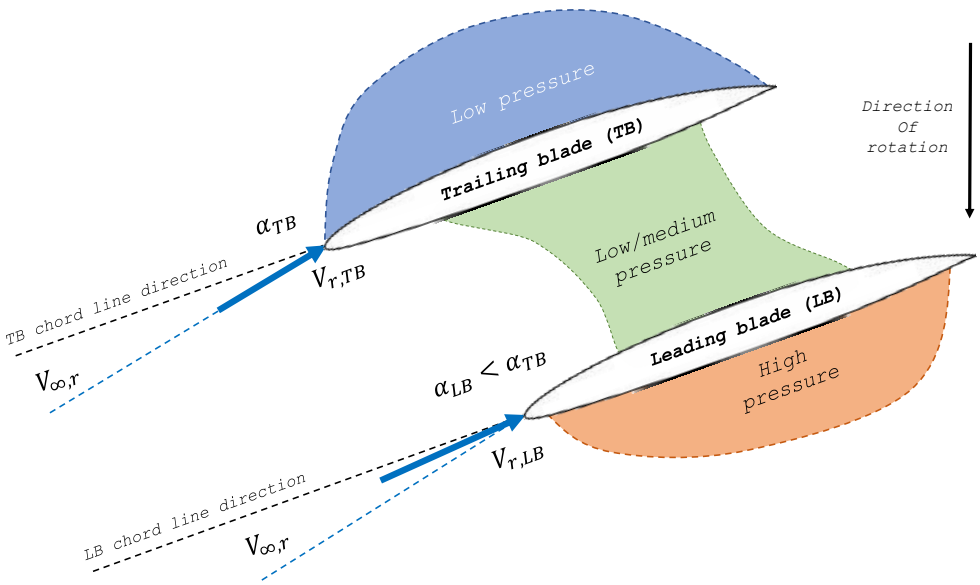

Figure 8.1.1: *Illustration of the encountered blade interference phenomena in a two-dimensional cut of the Boxblade. The blue arrows denote the relative flow velocities, and as can be seen, the LB angle-of-attack is affected by the flow from the TB, leading to lower loading. Also visible is the low/medium pressure region that can form in the blade passage.*

Bibliography

[1] 2036 Forecast Reveals Air Passengers Will Nearly Double to 7.8 Billion. https://www.iata.org/pressroom/pr/Pages/2017-10-24-01.aspx. Accessed: 2018-08-23.

[2] ICAO Long-Term Traffic Forecasts. https://www.icao.int/Meetings/aviationdataseminar/Documents/ICAO-Long-Term-Traffic-Forecasts-July-2016.pdf. Accessed: 2018-08-23.

[3] IATA Annual Review 2015. https://www.iata.org/about/Documents/iata-annual-review-2015.pdf. Accessed: 2016-05-16.

[4] IATA Annual Review 2017. https://www.iata.org/publications/Documents/iata-annual-review-2017.pdf. Accessed: 2018-08-22.

[5] Penner, J. E., Lister, D. H., Griggs, D. J., Dokken, D. J., and McFarland, M., 1999. *Aviation and the global atmosphere: Summary for policymakers*. Intergovernmental Panel on Climate Change.

[6] Lee, D. S., Fahey, D. W., Forster, P. M., Newton, P. J., Wit, R. C., Lim, L. L., Owen, B., and Sausen, R., 2009. "Aviation and global climate change in the 21st century". *Atmospheric Environment,* ***43***(22-23), pp. 3520–3537.

[7] Carbon offsetting for international aviation. https://www.iata.org/policy/environment/Documents/paper-offsetting-for-aviation.pdf. Accessed: 2018-08-27.

[8] Perez, R. E., and Jansen, P. W., 2017. "Coupled aircraft design and staging assignment for long–range operations". *Journal of Aerospace Operations*(Preprint), pp. 1–21.

[9] Larsson, L., 2014. *Analysis of concepts to reduce the environmental impact of aviation*. Chalmers University of Technology.

[10] Gierens, K., Lim, L., and Eleftheratos, K., 2008. "A review of various strategies for contrail avoidance". *The Open Atmospheric Science Journal,* ***2***, pp. 1–7.

[11] Bradley, M. K., and Droney, C. K., 2011. *Subsonic ultra green aircraft research: phase I final report*. National Aeronautics and Space Administration, Langley Research Center.

[12] NASA N+3, MIT Team, Final Review. http://aviationweek.typepad.com/files/mit_n3_final_presentation.pdf. Accessed: 2018-08-27.

[13] Thulin, O., 2017. "On the Analysis of Energy Efficient Aircraft Engines". PhD thesis, Chalmers University of Technology.

[14] NASA Armstrong Fact Sheet: NASA X-57 Maxwell. https://www.nasa.gov/centers/armstrong/news/FactSheets/FS-109.html. Accessed: 2018-08-27.

[15] Larsson, L., Grönstedt, T., and Kyprianidis, K. G., 2011. "Conceptual design and mission analysis for a geared turbofan and an open rotor configuration". In ASME 2011 Turbo Expo: Turbine Technical Conference and Exposition, American Society of Mechanical Engineers, pp. 359–370.

[16] Hager, R. D., and Vrabel, D., 1988. "Advanced turboprop project".

[17] Kinney, J. R., 2017. *The Power for Flight: NASA's Contributions to Aircraft Propulsion*.

[18] Arif Khalid, S., Lurie, D., Breeze-Stringfellow, A., Wood, T., Ramakrishnan, K., Paliath, U., Wojno, J., Janardan, B., Goerig, T., Opalski, A., and Barrett, J., 2014. Open rotor engine aeroacoustic technology final report. Tech. rep., General Electric Company, GE Aviation, One Neumann Way, Evendale, OH, United States.

[19] Zachariadis, A., Hall, C., and Parry, A. B., 2013. "Contrarotating open rotor operation for improved aerodynamics and noise at takeoff". *Journal of Turbomachinery,* ***135***(3), p. 031010.

[20] Stuermer, A., 2008. "Unsteady cfd simulations of contra-rotating propeller propulsion systems". In 44th AIAA/ASME/SAE/ASEE Joint Propulsion Conference & Exhibit, p. 5218.

[21] Negulescu, C. A., 2013. "Airbus AI-PX7 CROR Design Features and Aerodynamics". *SAE International Journal of Aerospace,* ***Vol. 6***(Issue: 2), pp. 626–642.

[22] Hall, C., Zachariadis, A., Brandvik, T., and Sohoni, N., 2014. "How to improve open rotor aerodynamics at cruise and take-off". *The Aeronautical Journal,* ***118***(1208), pp. 1103–1123.

[23] Van Zante, D. E., Collier, F., Orton, A., Khalid, S. A., Wojno, J. P., and Wood, T. H., 2014. "Progress in open rotor propulsors: The faa/ge/nasa open rotor test campaign". *The Aeronautical Journal,* ***118***(1208), pp. 1181–1213.

[24] Lepot, I., Leborgne, M., Schnell, R., Yin, J., Delattre, G., Falissard, F., and Talbotec, J., 2011. "Aero-mechanical optimization of a contra-rotating open rotor and assessment of its aerodynamic and acoustic characteristics". *Proceedings of the Institution of Mechanical Engineers, Part A: Journal of Power and Energy,* ***225***(7), pp. 850–863.

[25] Jaron, R., Moreau, A., Guérin, S., and Schnell, R., 2018. "Optimization of trailing-edge serrations to reduce open-rotor tonal interaction noise". *Journal of Fluids Engineering,* ***140***(2), p. 021201.

[26] Murphy, G. C., Gordon, B. J., Smith Jr, L. H., Schilling, J. C., and Stuart, A. R., 1993. Noise reduction in aircraft propellers, Mar. 2. US Patent 5,190,441.

[27] Hussain, Z. M., and Sheaf, C. T., 2011. Fluidfoil tip vortex disruption, Feb. 24. US Patent App. 12/851,776.

[28] Dejeu, C. M. M., Pascal, S., Talbotec, J., Leborgne, M., and Lepot, I. I. C., 2017. Propulsion device having unducted counter-rotating and coaxial rotors, Mar. 14. US Patent 9,593,582.

[29] Avellán, R. and Lundbladh. Air Propeller Arrangement and Aircraft. International Patent Application WO2011/081577A1, filed on Dec 28, 2009.

[30] Adriansson S., 2013. "Design and testing of a box-bladed propeller". Master's thesis, Chalmers University of Technology.

[31] Olofsson, J., and Pettersson, V., 2013. "Experimental investigation of an innovative high speed propeller". Master's thesis, Chalmers University of Technology.

[32] Lindsey, and Stevenson, 1948. Aerodynamics characteristics of 24 NACA 16-series airfoils at Mach numbers between 0.3 and 0.8, NACA-TN-1546. Tech. rep., National Advisory Committee for Aeronautics, Langley Aeronautical Lab, Langley Field, VA, United States.

[33] Adkins, C. N., and Liebeck, R. H., 1994. "Design of optimum propellers". *Journal of Propulsion and Power,* ***10***(5), pp. 676–682.

[34] Drela, M., 2006. "Qprop formulation". *Massachusetts Inst. of Technology Aeronautics and Astronautics, Cambridge, MA*.

[35] Ellbrant, L., Eriksson, L.-E., and Mårtensson, H., 2012. "Design of compressor blades considering efficiency and stability using cfd based optimization". In ASME Turbo Expo 2012: Turbine Technical Conference and Exposition, American Society of Mechanical Engineers, pp. 371–382.

[36] Ellbrant, L., Eriksson, L.-E., and Mårtensson, H., 2012. "Cfd optimization of a transonic compressor using multiobjective ga and metamodels". In Proceedings of the 28th International Congress of the Aeronautical Sciences, pp. 23–28.

[37] Lejon, M., Andersson, N., Grönstedt, T., Ellbrant, L., and Mårtensson, H., 2016. "Optimization of robust transonic compressor blades". In ASME Turbo Expo 2016: Turbomachinery Technical Conference and Exposition, American Society of Mechanical Engineers, pp. V02CT45A022–V02CT45A022.

[38] Violette, J.A., Sullivan, W.E., and Turnberg, J.E., 1984. Large-Scale Advanced Prop-Fan (LAP) blade design. Tech. rep., Hamilton Standard, Windsor Locks, CT, United States. Paper No. NACA-CR-174790.

[39] McCormick, B. W., 1995. *Aerodynamics, aeronautics, and flight mechanics*, Vol. 2. Wiley New York.

[40] Larrabee, E. E., 1979. Practical design of minimum induced loss propellers. Tech. rep., SAE Technical Paper.

[41] Béchet, S., Negulescu, C. A., Chapin, V., and Simon, F., 2011. "Integration of cfd tools in aerodynamic design of contra-rotating propellers blades".

[42] Gonzalez-Martino, I., François, B., and Rodriguez, B., 2013. "A physical insight into counter-rotating open rotor in-plane loads". *21ème Congrès Français de Mécanique, 26 au 30 août 2013, Bordeaux, France (FR)*.

[43] Kobayakawa, M., and Onuma, H., 1985. "Propeller aerodynamic performance by vortex-lattice method". *Journal of aircraft,* ***22***(8), pp. 649–654.

[44] Versteeg, H. K., and Malalasekera, W., 2007. *An introduction to computational fluid dynamics: the finite volume method*. Pearson Education.

[45] ANSYS CFX Solver Theory Guide Version 17.0, ANSYS Inc. 2016. ANSYS Inc.

[46] VILLAR, G. M. "Aerodynamic optimization of high speed propellers".

[47] Deb, K., Pratap, A., Agarwal, S., and Meyarivan, T., 2002. "A fast and elitist multiobjective genetic algorithm: Nsga-ii". *IEEE transactions on evolutionary computation,* ***6***(2), pp. 182–197.

[48] Ellbrant, L., 2014. *Multi-objective CFD-based design method for axial compressors*. Chalmers University of Technology.

[49] Ellbrant, L., Eriksson, L.-E., and Mårtensson, H., 2013. "Balancing efficiency and stability in the design of transonic compressor stages". In ASME Turbo Expo 2013: Turbine Technical Conference and Exposition, American Society of Mechanical Engineers, pp. V06BT37A017–V06BT37A017.

[50] Lejon, M., Andersson, N., Ellbrant, L., and Mårtensson, H., 2015. "Cfd optimization of a transonic compressor stage with a large tip gap". In ISABE International Society for Air Breathing Engines, pp. 1–11.

[51] Lejon, M., Grönstedt, T., Glodic, N., Petrie-Repar, P., Genrup, M., and Mann, A., 2017. "Multidisciplinary design of a three stage high speed booster". In ASME Turbo Expo 2017: Turbomachinery Technical Conference and Exposition, American Society of Mechanical Engineers, pp. V02BT41A037–V02BT41A037.

[52] Denton, J. D., 1993. "Loss mechanisms in turbomachines". In ASME 1993 International Gas Turbine and Aeroengine Congress and Exposition, American Society of Mechanical Engineers, pp. V002T14A001–V002T14A001.

[53] Dixon, S. L., and Hall, C., 2010. *Fluid mechanics and thermodynamics of turbomachinery*. Butterworth-Heinemann.

[54] Miller, R., and Denton, J., 2012. "Loss mechanisms in turbomachines". *Cambridge Turbomachinery Course, University of Cambridge, Cambridge, UK*, pp. 79–116.

[55] Glauert, H., 1933. Wind tunnel interference on wings, bodies and airscrews. Tech. rep., Aeronautical Research Council London (United Kingdom).

[56] Drela, M., 2009. "Power balance in aerodynamic flows". *AIAA journal,* ***47***(7), pp. 1761–1771.

[57] Najafi-Yazidi, A., Brès, G. A., and Mongeau, L., 2011. "An acoustic analogy formulation for moving sources in uniformly moving media". *Proceedings of the Royal Society A, Mathematical, Physical and Engineering Sciences,* ***467***(2125), January, pp. 144–165.

[58] Lindblad, D., Montero Villar, G., Andersson, N., Capitao Patrao, A., Courty-Audren, S.-k., and Napias, G., 2018. "Aeroacoustic analysis of a counter rotating open rotor based on the harmonic balance method". In *2018 AIAA Aerospace Sciences Meeting*, AIAA Paper 2018-1004. Kissimmee, FL, 8-12 January.

[59] Hartman, E. P., and Biermann, D., 1938. "The aerodynamic characteristics of full-scale propellers having 2, 3, and 4 blades of clark y and raf 6 airfoil sections".

[60] Reid, E. G., 1949. The influence of blade-width distribution on propeller characteristics. Tech. rep., Stanford University, CA.

[61] Zachariadis, A., and Hall, C. A., 2011. "Application of a navier–stokes solver to the study of open rotor aerodynamics". *Journal of Turbomachinery,* ***133***(3), p. 031025.

[62] Stuermer, A., and Yin, J., 2009. "Low-speed aerodynamics and aeroacoustics of cror propulsion systems". In 15th AIAA/CEAS Aeroacoustics Conference (30th AIAA Aeroacoustics Conference), p. 3134.